Trabajo Fin de Máster en Astrofísica

The remarkable FIR morphologies of dusty high-redshift radio galaxies: mergers or dusty outflows?

Ana Jiménez Gallardo
Universidad de La Laguna

Junio de 2018

Tutor: Helmut Dannerbauer
Instituto de Astrofísica de Canarias

Resumen

Las galaxias más masivas del Universo local se encuentran en los centros de los cúmulos de galaxias, cuyos progenitores son los proto-cúmulos, sobre-densidades de galaxias masivas a alto redshift. Por otra parte, se piensa que los progenitores de estas galaxias son las radio-galaxias a alto redshift (High-redshift Radio Galaxies o HzRGs). De esta forma, es posible encontrar proto-cúmulos mediante la búsqueda de HzRGs y, así, estudiar las predicciones de los modelos cosmológicos e investigar los procesos por los que evolucionan las galaxias más masivas del Universo local.

Las HzRGs son radio-galaxias a redshifts mayores que 2 con Núcleos Galácticos Activos (AGNs). Se consideran las galaxias con formación estelar más masivas del Universo temprano y han sido estudiadas por numerosos autores, entre los que se incluyen Miley & De Breuck (2008), Stevens et al. (2003), Ivison et al. (2012), Papadopoulos et al. (2000) y Gullberg (2016). Apesar de ser muy útiles en el estudio de los modelos de evolución galáctica, muchas de sus propiedades todavía no han sido explicadas. Entre estas propiedades destaca la emisión extensa (entre 50 y 250 kpc) en longitudes de onda submilimétricas detectada por Stevens et al. (2003) en la mayoría de las HzRGs estudiadas en su trabajo. Entender el mecanismo que causa esta emisión es el objetivo principal de nuestro trabajo.

Para poder llegar a una conclusión acerca de la emisión submilimétrica extensa de las HzRGs, recurrimos a observaciones de la línea de CO (4-3) (que se usa como trazador del contenido de gas molecular de una galaxia) de la galaxia 6C 1909+72 a z = 3.5324 realizadas con el interferómetro de IRAM, NOEMA. Esta HzRG presenta la emisión submilimétrica más extensa de entre todas las galaxias estudiadas por Stevens et al. (2003) ($\sim$ 500 kpc), lo que hace de esta galaxia el caso de estudio más claro. El hecho de utilizar la transición (4-3) del CO en lugar de la transición (1-0) del CO se debe a que la emisión del continuo debida al efecto sincrotrón domina a las frecuencias de la línea de CO (1-0), lo que hace que la detección de esta línea sea especialmente difícil en HzRGs.

Los diferentes escenarios que consideramos en este trabajo como posibles causas de la emisión submilimétrica extensa de las HzRGs son:

1. La presencia de otra galaxia en la línea de visión de 6C 1909+72, lo que hace que la emisión de ambas galaxias se superponga; en cuyo caso, la línea de CO (4-3) se podría ajustar usando una única Gaussiana estrecha.

2. La fusión de dos o más componentes forma el sistema que observamos como 6C 1909+72, causando esta emisión extensa. En este caso, con la suficiente resolución espectral, podríamos observar las líneas de CO (4-3) correspondientes a cada una de las componentes del sistema, de forma que el ajuste del espectro requeriría más de una Gaussiana estrecha.

3. La presencia de importantes outflows de gas molecular y polvo en 6C 1909+72. En este último escenario, para ajustar la línea de CO (4-3) sería necesario emplear una Gaussiana ancha y, además, se observarían alas anchas a los lados de la línea.

Tras calibrar las observaciones, reducir los datos y subtraer el continuo del espectro, se observa una única línea de CO (4-3) que se puede ajustar usando un perfil Gaussiano con FWHM $\sim$ 700 km/s. Dado que la línea es estrecha y que no se observan alas anchas, siguiendo el criterio usado por Cicone et al. (2013), llegamos a la conclusión de que 6C 1909+72 no presenta outflows de gas molecular.

Por otra parte, comprobamos si el espectro podría reproducirse usando un modelo en el que 6C 1909+72 estuviese en realidad formada por dos componentes cuyas líneas de CO (4-3) no estuviesen resueltas, lo que implicaría que la emisión submilimétrica extensa se debería a la presencia de dos componentes en proceso de fusión. Para ello, recurrimos al uso de un algoritmo de búsqueda local, con el que encontramos distintas combinaciones de dos Gaussianas que reproducen el espectro observado. Las componentes que reproducen el espectro de 6C 1909+72 son similares entre ellas y presentan FWHMs entre 450 y 700 km/s, valores típicos para galaxias submilimétricas (SMGs). Sin embargo, no podemos concluir que 6C 1909+72 sea un sistema de dos componentes en proceso de fusión, ya que no se observan distintas líneas resueltas.

Finalmente, llegamos a la conclusión de que la emisión submilimétrica extensa de la HzRG 6C 1909+72 se debe bien a la presencia de otra galaxia en la línea de visión o bien a que la galaxia está pasando por un proceso de fusión entre distintas componentes.

Con el objetivo de completar nuestro estudio de 6C 1909+72, presentamos una compilación de los flujos de la galaxia en distintas longitudes de onda, así como una compilación de sus propiedades. Además de esto, presentamos las propiedades de distintas HzRGs que se han observado usando la línea de CO (4-3) con el objetivo de comparar la galaxia 6C 1909+72 con el resto de HzRGs. Asimismo, introducimos en la comparación otras galaxias con gran formación estelar a alto redshift: las Galaxias Submilimétricas (Submillimeter Galaxies o SMGs) y los Quásars (Quasi-Stellar Objects o QSOs), observados por Bothwell et al. (2013) y por Carilli & Walter (2013) respectivamente. Con esto, encontramos que las HzRGs y las SMGs parecen seguir las tendencias esperadas para galaxias con estallidos de formación estelar, lo que no se observa para las QSOs. Sin embargo, esto podría deberse al bajo número de galaxias en nuestra muestra o al uso de un incorrecto valor del factor de conversión de la luminosidad de la línea de CO (4-3) a la de la línea de CO (1-0), el ratio de temperaturas de brillo.

Utilizando las propiedades de las HzRGs recogidas de la literatura, comprobamos que el ratio de temperaturas de brillo varía de una HzRG a otra, aunque suele estar entorno a 1; es decir, el gas molecular en HzRGs está, en general, termalizado hasta $J_{up} = 4$. Además, este ratio es diferente para HzRGs, SMGs y QSOs, debido a las diferentes condiciones del gas molecular en cada tipo de galaxia; por lo que el uso del ratio obtenido por Bothwell et al. (2013) para SMGs ($\sim$ 0.5) en HzRGs hace que se sobreestime hasta en un factor 2 la luminosidad de la línea de CO (1-0) y, con ello, la masa del gas molecular; de ahí la importancia de la correcta determinación del ratio de temperaturas de brillo para las HzRGs.

Contents

1 Introduction

1.1 Motivation

High-redshift radio galaxies (HzRGs) are radio-loud galaxies at redshifts larger than 2 that host Active Galactive Nuclei and are considered the most massive star-forming galaxies in the Universe (see review by Miley & De Breuck, 2008).

HzRGs are currently considered indicators of high-density peaks in the early Universe in which protoclusters are formed (Stevens et al., 2003). These protoclusters (see review by Overzier, 2016) are the progenitors of galaxy clusters, the most massive structures in the local Universe, and they are composed by a collection of halos at the same redshift that will eventually merge to form the galaxy clusters (Muldrew, Hatch & Cooke, 2015). The concentration of these halos is diffused and there is not a clear central halo (Overzier, 2016).

Currently, one of the most used methods for finding protoclusters consists on using HzRGs as tracers. This method has been proved successful in works like Hayashi et al. (2012). In addition, other galaxy populations, like Sub-millimeter Galaxies (SMGs), have been also used successfully for the same purpose (e.g. Dannerbauer et al., 2014).

In that way, the study of HzRGs is an important tool in testing galaxy formation models (Stevens et al., 2003). Even so, there are many characteristics of HzRGs that still remain unexplained. One of these characteristics is the extended dust morphologies that some of them present.

Stevens et al. (2003) presented the distribution of the emission re-radiated by the dust in and around seven HzRGs on scales from 30 kpc to 1 Mpc using submillimeter imaging. As a result, they found an extent of the dust emission from 50 to 250 kpc, larger than the extension of the radio emission in most cases. They also found that this emission could be in the form of several partially resolved or merged clumps in some of the HzRGs (as in 6C 1909+72), while in others it followed a smoother distribution (seen for example in 4C 60.07). There are three possible models that would explain this extended emission:

1. Line-of-sight blends, i.e., the emission observed would actually be the joint emission from the HzRg and another galaxy superimposed in the line of sight.
2. Gas-rich mergers. In this scenario, the extended emission would be due to the merging of two or more components.
3. Metal-rich gas and dust entrained in collimated outflows.

To discern among these scenarios, we observed the CO (4-3) line transition of the HzRG 6C 1909+72 at $z = (3.5324 \pm 0.0006)$ using the IRAM NOEMA interferometer. The choice of 6C 1909+72 was motivated by the fact that it is the HzRG with the most extended submillimeter emission ($\sim$ 500 kpc) among the HzRGs studied by Stevens et al. (2003), which can be seen in Figure 2b, in this work, making 6C 1909+72 the most clear-cut case to find out the cause of this extended submm emission in HzRGs.

Although there exist previous observations of the CO (4-3) emission from 6C 199+72 by Ivison et al. (2012), these observations are not deep enough to be able to discern among these scenarios, hence the need for new observations with higher signal-to-noise ratio than the existing ones.

Lastly, we focus on the CO (4-3) line since the synchrotron component of the continuum emission dominates at the frequency of the CO (1-0) transition ($\sim$ 115 GHz) (Ivison et al., 2012). Furthermore, the CO (4-3) emission is expected to be around an order of magnitude stronger than the CO (1-0) emission (Ivison et al., 2012).

1.2 High-redshift Radio Galaxies

High-redshift radio galaxies (HzRGs) are radio-loud active galactic nuclei (AGN) hosts at $z > 2$ that have radio luminosities at rest-frame frequency 500 MHz of $L_{500\,\mathrm{MHz}} > 10^{27}$ W Hz^{-1} (Gull-

berg, 2016). They are thought to be the most massive star-forming galaxies (Miley & De Breuck, 2008) since:

- They have large near-IR luminosities, which imply that they are one of the most massive types of galaxies in the early Universe.

- They present clumpy UV continuum morphologies, that are expected for galaxies that have been formed through mergers.

- Their rest-frame UV and submillimeter SEDs indicate a strong star formation, with star-formation rates up to $\sim 10^3$ $M_\odot yr^{-1}$.

One of their peculiarities is their strong morphological evolution up to $z < 4.4$ at rest-frame optical wavelengths (van Breugel et al., 1998). At $z > 3$, HzRGs present relatively bright, compact components of ~ 10 kpc that are often aligned with the radio sources and surrounded by diffuse emission ($\sim 50 - 100$ kpc) (van Breugel et al., 1999). These components become smaller, more centrally concentrated and less aligned with the radio structure at $z < 3$ (van Breugel et al., 1999).

Due to the fact that their stellar populations are among the most massive known, HzRGs are often used to search for overdense regions in the early Universe. These regions are the progenitors of the galaxy clusters that host the most massive galaxies in the local Universe, i.e., the bright cluster galaxies (BCGs) and cD galaxies (Miley & De Breuck, 2008).

1.2.1 Active Galactic Nuclei

The emission of HzRGs is believed to come from supermassive black holes (SMBHs) that are accreting mass at the center of the host galaxies. These objects are known as active galactic nuclei (AGN).

There are several classes of AGNs according to their luminosity and their spectral characteristics. However, the different types of AGNs are currently explained as apparent variations in the physical properties of the galaxies due to differences in the viewing angle. This is known as the "Unified Model". A diagram of an AGN according to this model can be seen in Figure 1.

According to the Unified Model, an AGN consists of an accretion disk that surrounds a SMBH ($\gtrsim 10^6$ $M_\odot$). This accretion disk is the main source of the UV-optical non-thermal continuum. At distances of several hundred to several thousand gravitational radii ($R_{grav} = GM/c^2$, where M is the mass of the central BH, G is the gravitational constant and c is the speed of light) gas clouds with electron densities $\sim 10^{11}$ cm^{-3} can be found. These clouds are the source of the broad emission lines (FWHM $\sim 1500 - 10000$ km s^{-1}) that can be observed in the UV-optical spectra of some AGNs. This central engine is surrounded by a molecular torus which is the cause why the broad lines and the non-thermal continuum cannot be observed in the cases where the torus plane is aligned with the line of sight. At several hundreds to thousands of parsecs, there are low-density clouds in which the narrow emission lines (FWHM $\lesssim 300 - 800$ km s^{-1}) are generated. These clouds are generally constrained to lie along the system axis. In the case of radio-loud sources, there are also relativistic jets along the disk axis that cause the radio and x-ray emission through synchrotron and inverse Compton mechanisms. A more detailed explanation can be read in Peterson & Wilkes (2006).

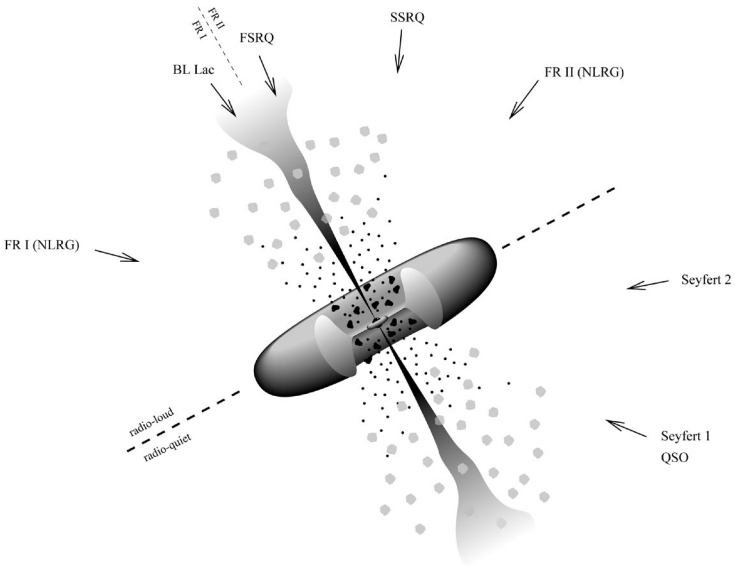

Figure 1: Diagram of the Unified Model of the AGNs. In this figure, the different components of the AGN as well as the different types of AGNs according to the viewing angle can be seen (Beckmann & Shrader, 2013). The figure is adapted from Torres (2004).

1.2.2 Molecular gas in high-redshift galaxies

Star formation is believed to occur in the interior of molecular gas clouds with high densities. The empirical description of the relation between the density of the star formation rate and the molecular gas density of a galaxy is known as the Schmidt-Kennicutt law and was introduced by Schmidt (1959) and Kennicutt (1989). Then, in order to get an estimate of the star formation rate (SFR) of a galaxy, we need to know its molecular gas contents.

The main component of the molecular gas clouds is H_2, which is also the fuel of star formation. However, since the H_2 does not have a permanent dipole moment, its rotational transitions do not emit easily observable lines in the millimeter (Bolatto, Wolfire & Leroy, 2013). That is why the carbon monoxide (CO) is often used as a tracer of molecular gas instead of H_2.

The reasons why the CO is one of the best tracers for molecular gas include the fact that it is produced in molecular clouds as a result of collisions with H_2, the fact that it is the second most abundant gas inside molecular clouds and the fact that it emits strongly at radio frequencies (Bolatto, Wolfire & Leroy, 2013). The CO transitions used in this work are $J = (1-0)$ at 115.2712 GHz and $J = (4-3)$ at 461.0407 GHz (Miley & De Breuck, 2008). Nevertheless, different transitions can be used to get a better understanding of the conditions of the gas in the galaxy since the low-J CO lines are better tracers of the diffuse and extended molecular gas, while the high-J CO lines trace the denser more compact molecular gas (Gullberg, 2016). In general, the transition that describes best the total molecular gas content of a galaxy is $J = (1-0)$, since it traces the more diffuse and cold molecular gas. However, observations of the CO (1-0) transition are difficult to carry out for HzRGs, due to the fact that the spectrum of these galaxies at the frequency of the line ($\sim$ 115 GHz) is dominated by the synchrotron part of the continuum emission (Ivison et al., 2012). In that way, observations of the CO (1-0) line are scarce among HzRGs.

The use of CO as a molecular gas tracer also leads to some problems. Some of the main issues are the destruction of the CO molecules at high-z by cosmic rays (Bisbas et al., 2015, 2017) and the need to establish a conversion factor from the CO luminosity to the H_2 mass.

Firstly, the destruction of the CO molecules caused by cosmic rays can deplete the CO content of molecular clouds, making them CO-invisible (Bibas et al., 2017). This situation would lead to a significant underestimation of the molecular gas content of the galaxy.

On the other hand, the conversion factor of the CO luminosity into H_2 mass is adopted according

to the type of galaxy considered and it relates the luminosity of the CO (1-0) line to the total molecular gas mass. For instance, for the Milky Way and the Local Group it is usually assumed a CO-to-H_2 factor: $\alpha_{CO} = 3 - 6$ $M_\odot$(K km $s^{-1}pc^2)^{-1}$ (Gullberg, 2016). In general, the typical values of this factor are $\alpha_{CO} \sim 4$ $M_\odot$(K km $s^{-1}pc^2)^{-1}$ for normal star-forming galaxies and $\alpha_{CO} \sim 0.8$ $M_\odot$(K km $s^{-1}pc^2)^{-1}$ for starburst galaxies and mergers (Gullberg, 2016). However, there is not a unique value that can be used for all the galaxies in the same evolutionary phase, so the choice of a fixed factor introduces an additional uncertainty in the results.

One thing to take into account is that this conversion factor is referred to the luminosity of the line of CO (1-0), so, in the cases where another transition is observed, it is important to transform the luminosity of this line to $L'_{CO\,(1\text{-}0)}$ in order to obtain the molecular gas mass. To make this transformation in high-z objects, the brightness temperature ratios, $r_{J+1,J/10}=\frac{L'_{CO\,(J,J+1)}}{L'_{CO\,(1\text{-}0)}}$, presented in Bothwell et al. (2013) are generally used.

Numerous observations of the CO emission lines have been made for different HzRGs. As a result, the masses of molecular gas obtained range from 10^{10} to 10^{11} $M_\odot$ (Miley & De Breuck, 2008). This means that there is still enough molecular gas to sustain future star formation in these galaxies.

The CO emission has been seen to extend over 10-20 kpc, although this can only be confirmed for the few cases in which the emission could be resolved (Miley & De Breuck, 2008). Moreover, in these observations, it was also seen the existence of alignments between the molecular gas and the radio morphologies that could be a result of jet-induced star formation (Miley & De Breuck, 2008). However, this is not always the case and more observations would be needed in order to get to a conclusion.

1.2.3 HzRG 6C 1909+72

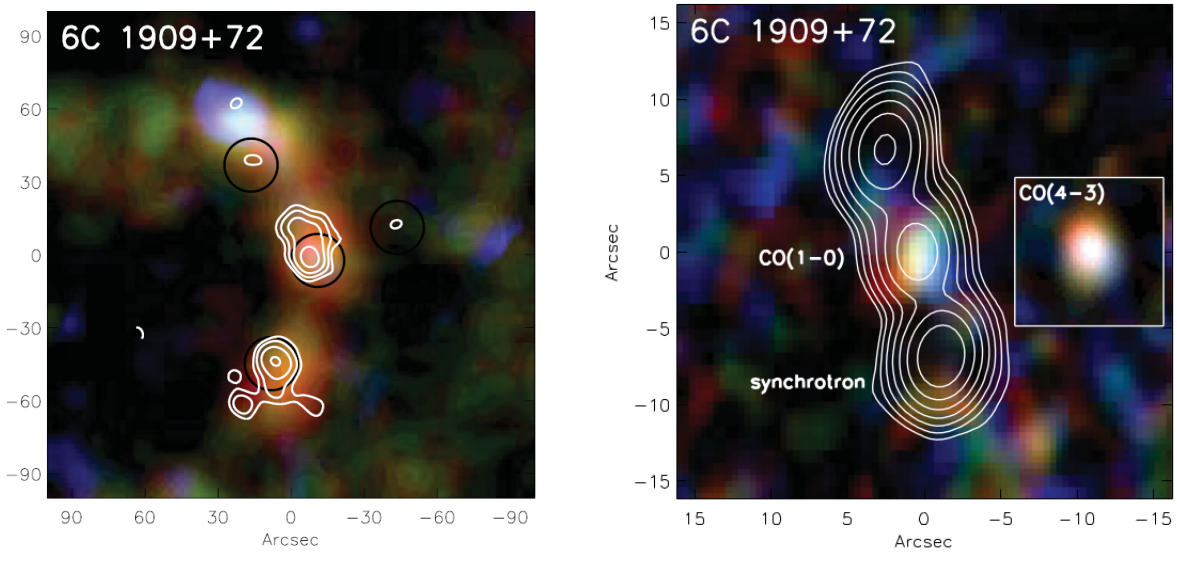

(a) (b)

Figure 2: Figure a: 850 μm continuum emission image from Stevens et al. (2003) with $\sqrt{2}$-spaced countours starting at 3σ superimposed to false-color images made with *Herschel* 160, 250 and 350 μm imaging from Ivison et al. (2012). The SMGs in the field of 6C 1909+72 identifed by Stevens et al. (2003) are marked with black circles. Figure b: False-color image of the CO (1-0) emission from 6C 1909+72 (the CO (4-3) emission can be seen in the inset of the figure) obtained from Ivison et al. (2012). The synchrotron emission is represented using isophotal contours at -3, 3, 6, 12, ... $\times$ the local noise level. These contours show the position of the jets of the galaxy.

This work is centered on the HzRG 6C 1909+72 at $z = (3.5324 \pm 0.0006)$, also known as 4C 72.26, TXS J1908+7220 and 8C 1909+722. This galaxy has been studied previously by authors like Stevens et al. (2003), Ivison et al. (2012), Papadopoulos et al. (2000) and Smith et al. (2010).

6C 1909+72 presents a very extended submillimeter emission co-aligned with the radio jets ($\sim$ 500 kpc, Ivison et al., 2012). In fact, it stands out among other HzRGs because its submm emission is one of the most extended that have been found for this kind of objects, what makes this galaxy a perfect candidate to study the origin of the extended submm emission in HzRGs, by discerning among the possible scenarios that could explain it:that the emission comes from the line-of-sight blend of the HzRG and another galaxy; that 6C 1909+72 is actually a merger system; and that the galaxy presents powerful molecular gas and dust outflows.

Another striking characteristic of 6C 1909+72 is the presence of three SMGs companions in its field reported by Stevens et al. (2003), as seen in Fig. 2a. This number of companions is higher than what could be expected according to "blank-field" surveys. These surveys suggest that the average number of submillimeter sources per SCUBA field at a flux level of $S_{850} > 5 - 6$ mJy is around one. Moreover, one of these companions is much brighter than normal, with $S_{850} > 20$ mJy (Stevens et al., 2003). However, despite the brightness of this SMG, Ivison et al. (2012) failed to detect its CO (1-0) emission. This lead to the conclusion that the presence of this bright SMG in the same field as the HzRG could be due to the chance alignment of distant starbursts, instead of them being physically related.

Although Dey (1997) classified 6C 1909+72 as a broad-absorption-line radio galaxy due to its broad absorption features; Smith et al. (2010), using UV spectroscopy, argue that 6C 1901+72 is, in fact, a system of two vigorously star-forming galaxies separated by 1300 $\pm$ 200 km s^{-1}, both displaying P-Cygni-like absorption line profiles. One of the two galaxies would be the AGN host and the source of the *Lyα* emission, that could be interpreted as a galaxy-wide superwind.

1.3 Radio Interferometry

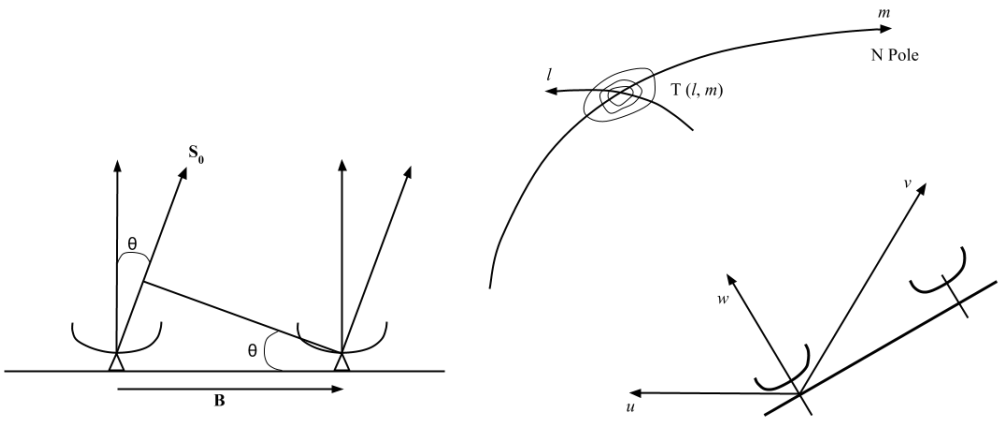

Figure 3: The figure on the left is a schematic diagram of a two element interferometer obtained from Wilner (2005). The interferometer in this diagram is formed by two antennas, separated by a distance B, the baseline, and oriented towards a source in the direction of the unitary vector $\hat{s}_0$. The figure on the right is a diagram of an interferometer obtained from Wilner (2005). In this diagram, the different components of the vectors $\frac{\vec{B}}{\lambda}$ and $\hat{s}$ as explained in the text can be seen. Here, $T\,(l,\, m)$ represents the perceived sky.

Interferometry is a very useful observational technique in sub-millimeter and radioastronomy. Its importance resides in the fact that using signals from different antennas combined provides a

much better angular resolution than the one that could be attained with a single antenna.
Since the angular resolution of an optical system is given by:

$$\theta(\text{arcsec}) = 2.5 \cdot 10^5 \frac{\lambda}{D} \tag{1.1}$$

in general, to get a better angular resolution it is needed a larger diameter. However, at longer wavelengths, the diameters of the telescope needed to get a good angular resolution are too big to be feasible. That is why an array of antennas is used instead of just one, achieving the resolution of a telescope with a diameter equal to the distance between the antennas, but with a collective area equal to the sum of the collective areas of all of the antennas. The distance between any pair of antennas is known as the baseline, B. A schematic diagram of a two antennae interferometer can be seen in Figure 3.

The functioning of an interferometer is based on the measure of the coherence level of the signal resultant by combining the signals from different antennas that are observing the same source. The differences in the phases measured in each antenna are due to the difference in the times of the reception of the signal in each antenna. This difference in the time of the reception of the signal is called the geometrical delay, τ_g, and can be expressed as:

$$\tau_g = \frac{\overrightarrow{B} \cdot \hat{s}}{c} \tag{1.2}$$

where $\overrightarrow{B}$ is the baseline vector, $\hat{s}$ is the unitary vector in the direction of the source and c is the speed of the light.

1.3.1 Response of an interferometer

The method for deriving the response of an interferometer presented here is a simplified version of the explanation shown in Chapter 15 of the third edition of Thompson, Moran & Swenson (2017).

The response of an interferometer over the whole sky, taking into account the effects of the primary beams of the antennas, is known as the visibility, $V_\nu(u, v)$. The visibility of an interferometer depends on the orientation of the antennas with respect to the baselines, on the flux density of the source and on the frequency of the observation. The simpler example is the one of an interferometer formed by two elements, i and j, observing an isolated source with spectrum S_ν. In that case, the visibility will be $V_{ij}(\nu) = S_\nu \phi$, where ϕ is the difference in phase between the antennas.

The difference in phase between the antennas can be written as: $\phi = \mathrm{e}^{-2\pi i \frac{\vec{B}\cdot\hat{s}}{\lambda}} = \mathrm{e}^{-2\pi i \tau \nu}$, where ν is the frequency, and λ is the wavelength of the incident radiation.

Now, calling $\frac{\vec{B}}{\lambda} = (u, v, w)$, where u, v and w are the components of the baseline vector in units of wavelengths in the East-West direction, the North-South direction and the up-down direction respectively; and $\hat{s} = \left(l, m, \sqrt{1 - l^2 - m^2}\right)$ (Figure 3) and making the usual approximation that all the antennas are in the same plane with respect to the source ($w = 0$), we can write the phase as:

$$\phi = \mathrm{e}^{-2\pi i(ul + vm)} \tag{1.3}$$

Then, the response of an interferometer over the whole sky, taking into account the effects of the primary beam can be written as:

$$V_\nu(u, v) = \int\int A(l, m)\, I_\nu(l, m)\, \mathrm{e}^{-2\pi i(ul + vm)} dl dm \tag{1.4}$$

where $A(l, m)$ is the product of the primary beams of the antennas and $I_\nu(l, m)$ is the sky brightness distribution. From now on, we will rename this product as $T_\nu(l, m) = A(l, m)\, I_\nu(l, m)$, in such a way that T_ν will be the sky brightness distribution taking into account the effect of the

primary beams of the antennas, i.e. the perceived sky. A diagram of the situation can be seen in Figure 3. It is important to highlight that, while the phase is a term inherently dependent on the baseline, the perceived sky does not depend on the baseline, but on the antenna design.

As seen from this expression, the visibility is the Fourier transform of the sky brightness distribution and vice-versa, the sky brightness distribution can be obtained by doing the inverse Fourier transform to the visibility. The domain of the visibilities is usually called the uv-plane.

1.3.2 Aperture Synthesis

To synthesize a large aperture antenna using the interferometer it is necessary to sample the visibility at enough points of the uv-plane. The synthesized antenna will have the size corresponding to (u_{max}, v_{max}) (Wilner, 2005). The better the sampling of the uv-plane, the easier and more precise is the reconstruction of the sky brightness from the visibilities, as can be seen in Figure 4.

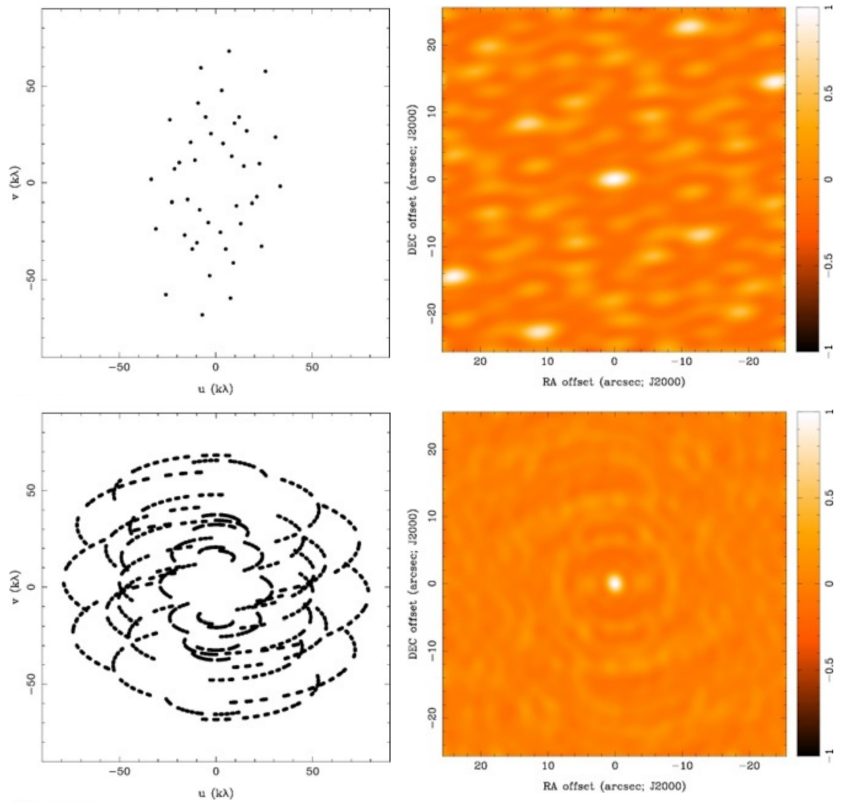

Figure 4: The upper figure shows the sampling of the uv-plane done using 7 antennas and one sampling and the image of a point source obtained from that observation by Fourier Transforming the visibilities. On the other hand, the lower figure shows the sampling done using the same 7 antennas but during a period of 8 hours, using Earth-Rotation synthesis as explained below. It can be seen that the image resulting from this sampling improves considerably in contrast to the one obtained with a worst sampling of the uv-plane.

Nevertheless, each pair of antennas with a fixed baseline provides two samples of the uv-plane (one for each possible direction of the baseline vector, i.e. from antenna 1 to antenna 2 or from 2 to 1) (Wilner, 2005). So, to get a better sampling of the uv-plane, there are two possibilities: increasing the number of antennas of the array, which can only be done until all the antennas available in the array are in use, or changing the baselines of the array. This last option is the more feasible and can be done by physically changing the configuration of the array or by using the Earth rotation.

This last technique is called Earth-Rotation Synthesis Imaging and it was described by Sir Martin

Ryle (1962), who received the 1974 Nobel Prize in Physics for the development of this technique. It is based on the change of the baseline as seen by the sky with the rotation of the Earth. A diagram illustrating how the baselines change with the rotation of the Earth can be seen in Figure 5. Using this technique an observation of 12 h in the same array configuration provides enough samples to form complete ellipses in the uv-plane, one for each pair of antennas. However, in reality, these ellipses have gaps due to different effects, like stopping the observations to take calibrations or due to technical or meteorological problems.

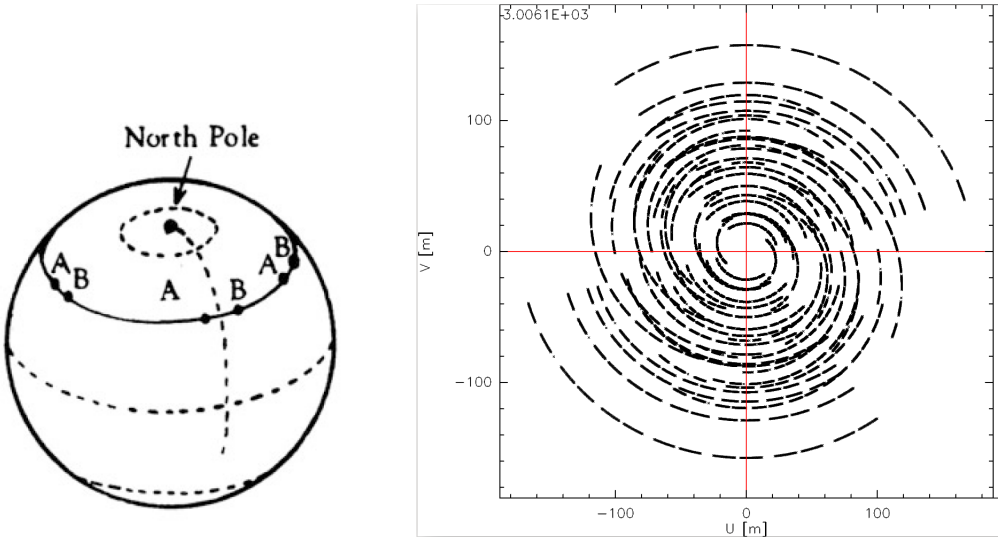

Figure 5: The figure on the left is a diagram obtained from Thompson, Moran & Swenson (2017) that shows the change of the baselines as seen from the source due to the rotation of the Earth. This technique provides a much better sampling of the uv-plane that the one that could be obtained just by changing the array configuration. The figure on the right represents the coverage of the uv-plane obtained during our observations using Earth-rotation synthesis with an array of 8 antennas during 8 h. This is a example of what is considered a good coverage of the uv-plane.

The coverage of the uv-plane obtained using Earth-Rotation Synthesis during our observations can be seen in Figure 5.

1.3.3 Imaging

Since the uv-plane is not completely sampled, the response of the interferometer will not be directly the visibilities, V_ν, but the visibilities multiplied by the sampling pattern, S. Then, doing the Fourier transform of the response of the interferometer will not give directly the perceived sky, T_ν, but the perceived sky convolved with the Fourier transform of the sampling pattern, s. This function is known as the point spread function or as the "dirty beam" and the image resulting from the convolution of the perceived sky with the dirty beam is called "dirty image", $T_\nu^D\,(l,\,m)$ (1.5). The description of the imaging can be found in more detail in Wilner (2005).

$$\mathcal{F}(V_\nu\,(u,\,v)\cdot S\,(u,\,v)) = T_\nu\,(l,\,m) * \mathcal{F}(S\,(u,\,v)) = T_\nu\,(l,\,m) * s\,(l,\,m) = T_\nu^D\,(l,\,m) \tag{1.5}$$

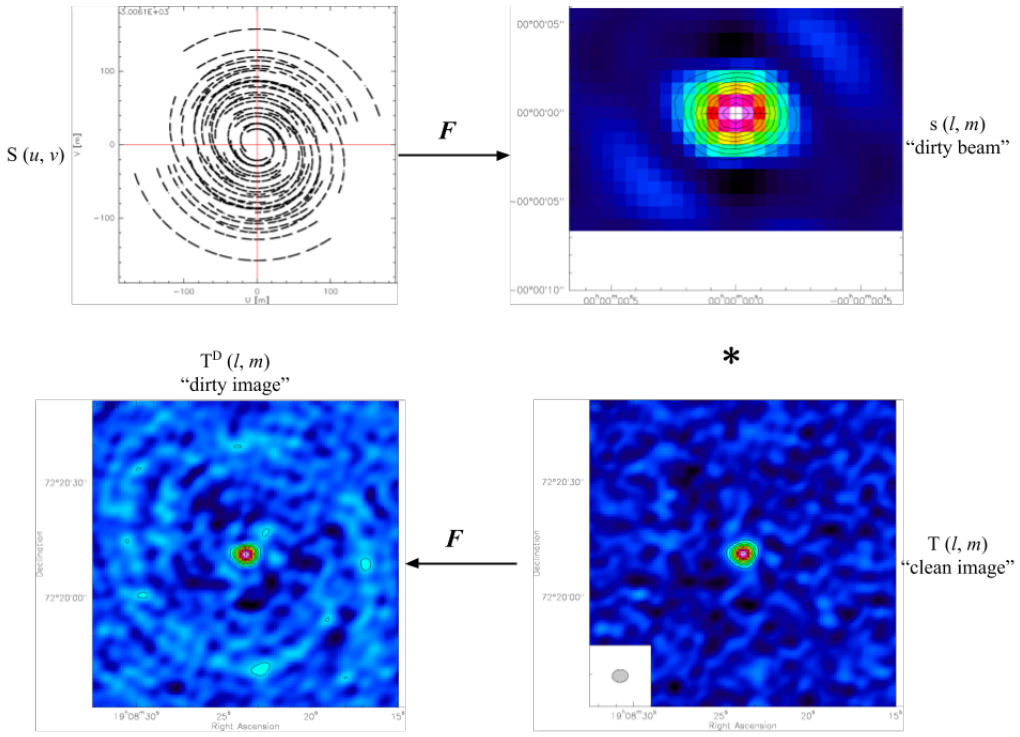

Figure 6: Images that can be obtained using our interferometry observations. In this image, $S\,(u,\,v)$ is the sampling pattern, which Fourier transform is the dirty beam seen at its right, $s(l,\,m)$. The convolution of the dirty beam with the sky brightness distribution, $T(l,\,m)$, gives as a result the dirty image ($T^D\,(l,\,m)$).

An example of the images that can be obtained as described above can be seen in Figure 6. Since the resultant image is convolved with the dirty beam, in order to obtain the closest possible result to the true brightness distribution it is needed to carry out a process that is known as cleaning (Wilner, 2005). This process uses the dirty image, the dirty beam and some assumptions about the energy distribution of the source to obtain a "clean image". For example, the dominant deconvolution algorithm and the one used in this work is called "clean" and assumes that $T_\nu\,(l,\,m)$ is a collection of point sources. This algorithm was first described by Högbom in 1974. A comparison between the dirty image and the "clean image" obtained using the clean algorithm can be seen in Figure 7. The main issue of using the cleaning algorithm is that it does not assure that the flux of the dirty image is maintained in the clean image. That is the reason why the clean image is not used to carry out measures of the flux.

It is important to take into account that there is not a unique image compatible with a certain set of visibilities and the final image obtained is determined by the parameters chosen for the deconvolution (Wilner, 2005). Moreover, the existence of missing or wrong visibilities has an influence on the whole image, since, as seen in equation (1.4), the visibility in a point of the uv-plane is the result of doing an integral over the whole sky (Wilner, 2005).

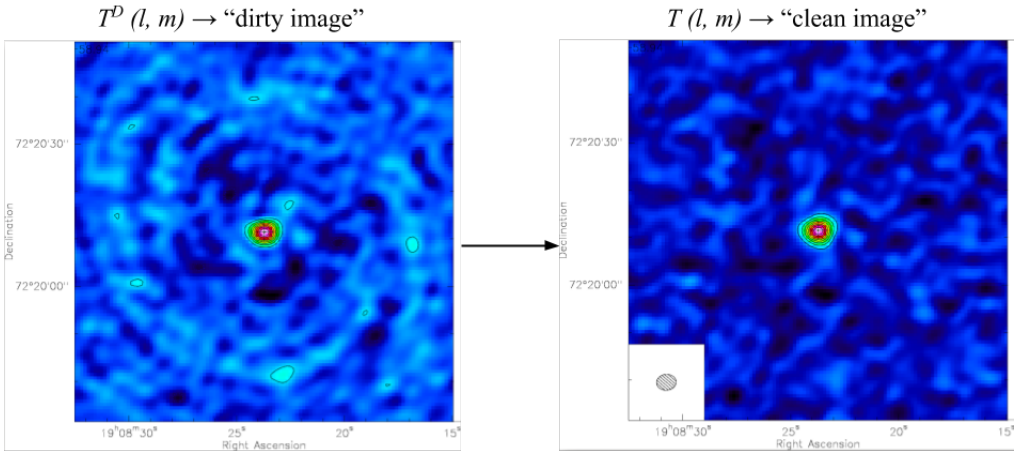

Figure 7: Example of the result of the clean algorithm compared to the dirty image obtained from our obervations. This final image depends on the parameters used in the convolution as well as the coverage of the uv-plane, but it is not the only possible solution since there are infinite numbers of images compatible with the visibilities and an uneven coverage of the uv-plane has impact on the whole image. The images represent the CO (4-3) line emission of the HzRG C 1909+72. The effect of the beam can be seen crearly on the dirty map, hence the importance of the cleaning algorithm. At the bottom left corner of the clan image, it can be seen the size of the clean beam.

1.3.4 NOEMA

The data used in this work was taken using the NOEMA[1] (NOrthern Extended Millimeter Array) Interferometer from IRAM (Institut de Radioastronomie Millimétrique) (Figure 8), situated on the Plateau de Bure at 2550 m altitude in the French Alps. It is a nine-antenna array with baselines of up to 760 m and it is currently the most advanced millimeter array in the North Hemisphere. It is located at a latitude of 05°54'28.5" and a longitude of 44°38'02.0" (Neri, 2016). The interferometer is still undergoing a process of ampliation that is expected to end by 2020 with the addition of three more antennas. The observations are typically carried out in service mode.

Each antenna is a 15 m diameter telescope with a Cassegrain focus and they each can observe in dual polarization in the 3 mm, 2 mm, 1.3 mm and 850 μm atmospheric windows (Neri, 2016).

The antennas are positioned along a "T" shaped track, where the north-south arm is 368 m long and the east-west arm extends 216 m west and 544 m east of the intersection. The separation between the antennas can be changed up to a maximum separation of 760 m in the east-west arm. This separation allows to get an angular resolution of 0.5 arcsec at 1.3 mm (230 GHz). This configuration of the antennas can be seen in Figure 8.

The data reduction, calibration, and creation of the maps is carried out using the software contained in the GILDAS package, provided by IRAM.

[1] http://www.iram-institute.org/

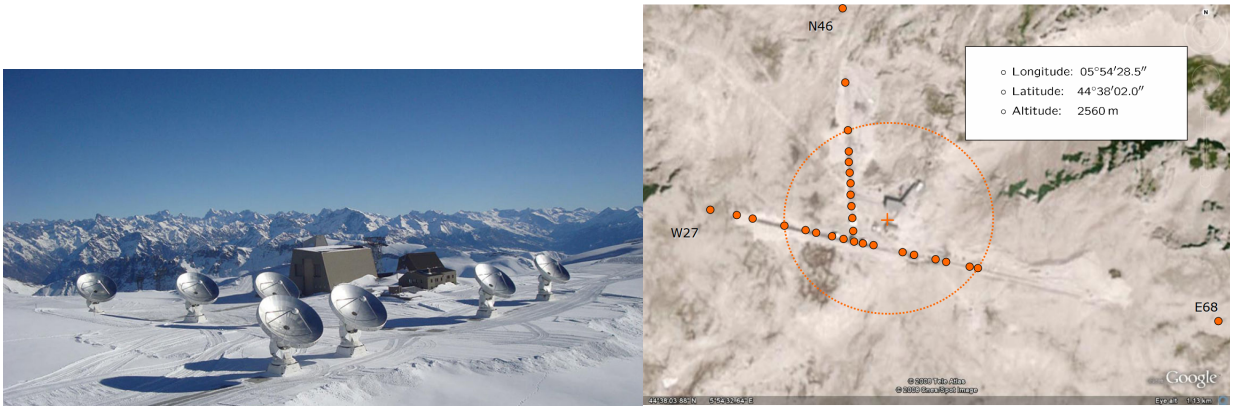

Figure 8: The image on the left is a photo of the NOEMA interferometer. The image on the right represents the possible positions of the antennas in each of the tracks of the array (Neri, 2016).

2 Observations and Calibrations

2.1 Observations

The observations of the ^{12}CO (4-3) transition ($\nu_{obs} = 101.721$ GHz) from 6C 1909+72, at $z = 3.5324$, used in this work were obtained using the NOEMA interferometer on the 12th of July 2017 (Proposal ID: S17BZ, P.I.: H. Dannerbauer). More specifically, they were obtained using the interferometric imaging mode in the 8D configuration of the array; i.e. the compact configuration[2]; in the 3-mm atmospheric window. This configuration is the best suited for detection experiments.

These observations were carried out by IRAM staff ; while the data calibration was made by me as part of this work. They are centered around $\nu_{obs} = 101.721$ GHz with a bandwidth of 3.613 GHz. By binning these observations into 180 channels with widths of $\simeq 60$ km s^{-1}, the spectral resolution of the observations is $\simeq 20$ MHz.

The observations were made in a unique track of ~ 8.3 h distributed among 667 scans of 45 s. Originally, the planned total on-source integration time was 14 h, but the track was shortened since the signal-to-noise ratio proposed was achieved earlier. Even so, the uv-plane was well-sampled (Figure 5).

The unstable atmospheric conditions were the cause why the last three hours of the observations had to be flagged; i.e., the data could not be used. In that way, the total non-flagged integration time was ~ 5.3 h distributed among 421 scans of 45 s. We also rejected scans with a phase RMS larger than 40° as it will be explained in the following sections.

Lastly, the bandpass, phase and amplitude calibrators used were the quasars 2013+370 and 1849+670 and 1928+738, respectively. The binary star MWC349 was used as the reference for the flux. The calibrations will be explained in more detail in the following section. The calibrations and data reduction were carried out using the IRAM software, GILDAS[3].

The residual phase loss was $\leq 60°$, while the residual amplitude loss was $\leq 20\%$. The pointing error was $\leq 40\% \simeq 19.8''$, the focus error was $\leq 30\% \simeq 0.9$ mm and the tracking error was $\leq 10\% \simeq 5''$.

2.2 Data Reduction

The calibration process is needed due to the fact that electronics have variable gains and, more importantly, due to the atmospheric absorption and variability, that causes fluctuations on the

[2]http://www.iram.fr/IRAMFR/GILDAS/doc/html/noema-intro-html/node4.html
[3]http://www.iram.fr/IRAMFR/GILDAS/

flux and on the path length and, therefore, fluctuations in the phase of the signal (Gueth, 2016). The most important effects of the atmosphere are:

- Its thermal emission, that causes an increment in the noise of the signal.
- Its absorption, that causes an attenuation of the signal received.
- Its variability, that introduces a phase error dependent on time.

On the other hand, the main calibration related to the antennas is the calibration of the temporal effect on the visibilities, which is mostly due to the different antenna gains.

The observed visibilities can be written as:

$$V_{ij}^{obs}(\nu,\ t) = G_{ij}(\nu,\ t)V_{ij}(\nu,\ t) + noise \tag{2.1}$$

where $G_{ij}(\nu,\ t)$ are the complex gains (that are mostly antenna-based) and $V_{ij}(\nu,\ t)$ is the true visibility (Gueth, 2016). Assuming that the gains are only antenna-based, i.e. assuming that the effect of the baselines in the gains is negligible, the visibilities can be written as:

$$V_{ij}^{obs} = G_{ij}V_{ij} = g_i g_j V_{ij} \tag{2.2}$$

where g_i and g_j are the individual gains of antennas i and j. With this approximation, by observing a source with a known flux, we obtain a system of $N(N-1)/2$ equations (one per baseline) and N unknown, so we can obtain the gains of all the antennas by doing a least squares minimization (Gueth, 2016).

It is important to take into account that apart from the calibrations described in this text that were carried out by me, "real-time calibrations" have to be done at the same time as the observations and are carried out. These calibrations include the pointing, focus, baselines, and cable phase calibrations (Piétu, 2016). Furthermore, during the target observations, the calibrators were observed periodically.

The calibrations are carried out using the GILDAS software package[4]. GILDAS is the IRAM data reduction package. It is specifically oriented towards spectral line mapping and was developed by the Groupe d'Astrophysique de Grenoble (or, as it is currently known, the Laboratoire d'Astronomie de l'Observatoire de Grenoble). GILDAS is composed by the following packages: GREG, which is a 1-D and 2-D graphic program; CLASS, for single-dish data processing; ASTRO, which is used to prepare the observations; CLIC, for interferometric data processing; and MAPPING, an imaging and deconvolution package of interferometric data.

In particular, the tool we used to do the calibrations is CLIC and the steps we followed to carry out the calibrations in this work are described in the following subsection. These steps can also be found at Gueth (2016).

The calibrations that we carried out in order to obtain our final image are the following:

1. Atmospheric Phase Correction (called Phcorr on CLIC): This process determines whether the real-time atmospheric correction is improving the data or not by comparing the corrected and uncorrected amplitude of the calibrator to check if the atmospheric correction restores the amplitude expected for the calibrator (Piétu, 2012). It allows the user to select whether they want to apply the correction. In our case, this correction was needed and improved significantly the data due to the unstable atmospheric conditions at the time of the observations.

2. Bandpass calibration (Gueth, 2016) (called RF on CLIC): It is used to determine the change of the phase and the amplitude with the frequency introduced by the instruments and to subtract this effect from the data. To do that, a point-source with a continuum emission,

[4] http://www.iram.fr/IRAMFR/GILDAS/

usually a quasar, is observed at the beginning of each project and the amplitude and the phase are fitted as a function of the frequency, as seen in Figure 10a. The reason behind choosing a point-source with continuum emission is that a point-source has phase zero and a source with continuum emission presents a constant amplitude versus frequency. Then, knowing that and with the observations from the interferometer, the effect of the bandpass can be removed from the data. The calibrator used for this step was the quasar 2013+370.

3. Phase calibration (Gueth, 2016) (called Phase on CLIC): Since the variations of the phase occur at different timescales (for example, the atmosphere causes short-term time variations of the phase, while the variations caused by antenna position errors have a periodicity $\sim$ 24 h), the calibrator needs to be observed during the observations. In this case, the calibrator is also a point-source (usually a quasar), so that its phase is zero. Then, the phase is fitted as a function of time using a spline, as seen in Figure 10b. The correction to the phase obtained is applied to the rest of the data. The calibrator used in this step was the quasars 1849+670 and 1928+738.

4. Absolute Flux calibration (Castro-Carrizo, 2016) (called Flux on CLIC): This calibration is used to calibrate the fluxes of the point-sources that will work as amplitude calibrators, due to the fact that the fluxes of the calibrators usually change with time, so an antenna efficiency (the factor that relates the antenna temperature with the flux from the source) obtained directly with these calibrators would not be reliable. Instead, a bright radio star with well-known emission, usually MWC349 as in our case, is used as a reference calibrator. The value of the flux of this calibrator is already fixed, so by representing its amplitude versus time, the antenna efficiencies can be obtained, as seen in Figure 10c. Once the antenna efficiencies are obtained, the flux for the other calibrators (point-sources) can be found. The antenna efficiencies obtained in these way are not influenced by the time variability of the calibrators, although they do present temporal variations. These variations are introduced by the atmosphere and by instrumental effects and can be corrected using the amplitude calibration.

5. Amplitude calibration (Gueth, 2016) (called AMPL on CLIC): Once the fluxes of the calibrators are obtained using the Absolute Flux calibration, we need to calibrate out the temporal variations of the antenna efficiencies by fitting the amplitude of these calibrators as a function of time, as seen in Figure 10d. The function obtained from the fit can be used to remove the variations of the amplitude with time introduced by the antenna and the atmosphere in the data. The calibrator used for this step was the same that the calibrator used for the phase calibration, the quasars 1849+670 and 1928+738.

Once these steps have been followed, we use the procedure called "Data Quality Assesment"[5]. This procedure allows us to flag the data that does not satisfy certain quality criteria predefined by us using the widget shown in Figure 9. The quality criteria that can be chosen are the maximum phase RMS, seeing, amplitude loss, point correction, focus correction and tracking RMS for our data. Changing these parameters affects the signal-to-noise ratio of the calibrated data as it will be discussed in the results section. In particular, the main criterion to assess the quality of the data is the phase stability. At the end of the procedure, histograms that present the analysis of the data quality are written, as seen in Figures 11a and 11b.

The calibrations were applied consecutively using CLIC, Standard calibration widget shown in Figure 9. The calibrations are applied in order from left to right.

[5]https://www.iram.fr/IRAMFR/GILDAS/doc/html/pdbi-cookbook-html/pdbi-cookbook.html

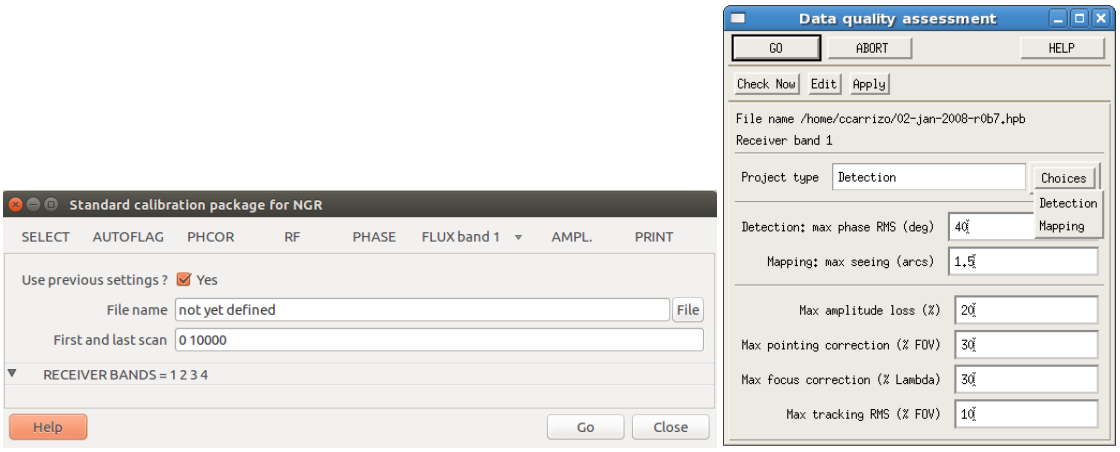

Figure 9: On the left, the standard calibration widget. The calibrations are applied in the order seen in the widget from left to right. On the right, the widget of the Data quality assessment is shown. Here, it can be seen the parameters that can be changed.

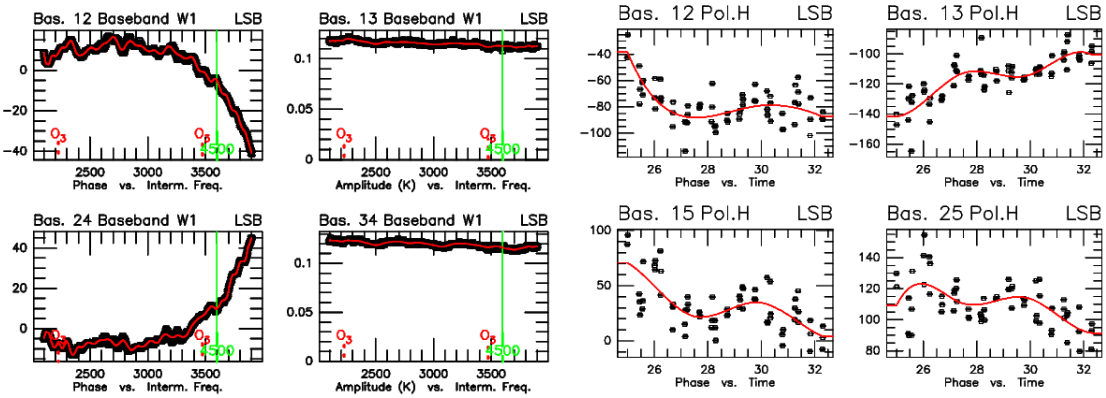

(a) (b)

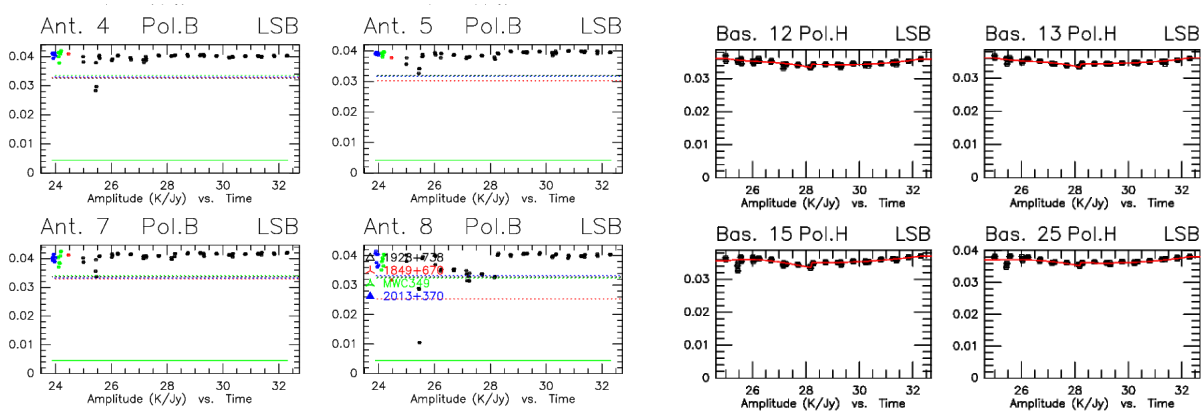

(c) (d)

Figure 10: Examples of the different plots obtained from the different calibration steps. Figure a: Example of the bandpass calibration for some of the baselines. The amplitude is plotted as a function of the frequency introduced by the instrument. Figure b: Example of the phase calibration for some of the baselines. The phase is represented as a function of the time. Figure c: Example of the absolute flux calibration for some antennas. The amplitude of the flux calibrator (green dots) is represented as a function of time and compared to the model of its flux (green dotted line). Figure d: Example of the amplitude calibration for some of the baselines. The amplitude is represented as a function of the time.

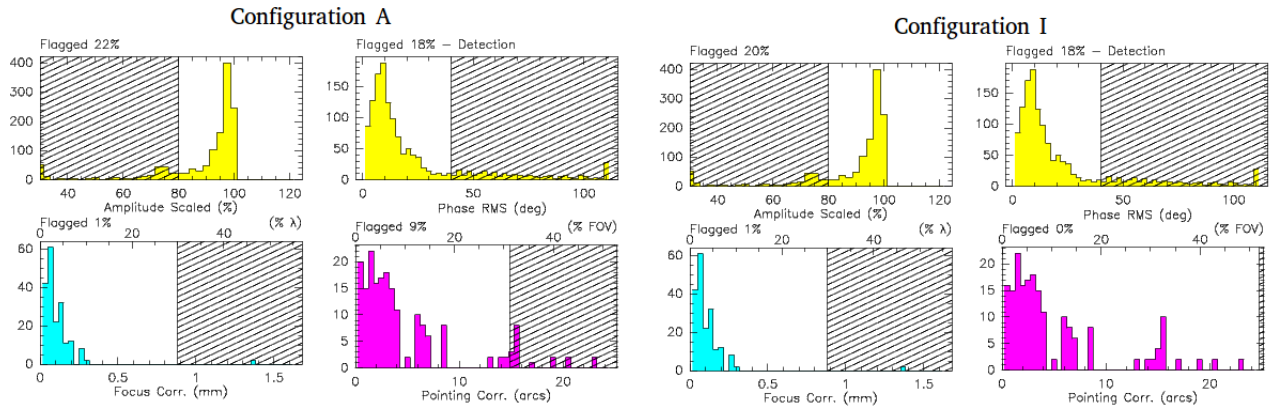

(a) (b)

Figure 11: Comparison between the histograms resulting from the Data Quality Assessment using configurations A (Figure a) and I (Figure b) from Table 1. The flagged percentage of the visibilities is represented by the shadowed area and can be changed by changing the parameters in the Data Quality Assessment procedure.

To create the uv-maps, seen in Figure 12, first, a uv-table has to be written using CLIC. This table contains all the calibrated source visibilities and, once it has been created, can be used to do direct calculations (like plotting the coverage map, plotting the amplitude vs uv-radii or fitting the Fourier Transform of a given function to the uv-data to obtain the flux) or to create the uv-maps. All these options are available in the GILDAS tool, MAPPING.

Using MAPPING, one can create the uv-map just by using the command “go uvmap”. This command does the Fourier Transform of the visibilities from the uv-table, obtaining the dirty image.

Lastly, to obtain the clean map, we use the command “go clean” from MAPPING that is based on the Högbom algorithm as described in Section 1.3.3 and that assumes a model of a point source in order to be able to do the deconvolution of the dirty beam from the dirty image. With that, the clean maps were obtained.

The cleaning process can introduce changes in the flux because of the deconvolution process and the assumption of a model for the source. On the other hand, the effect of the sidelobes is mitigated in the clean image, so the distribution of the emission is more accurate in this image than in the dirty image. That is why the clean image is used only to get a visual representation of the emission from the galaxy; while the fluxes and the spectrum were obtained directly from the uv-table, by Fourier Transforming the visibilities and assuming a point source model.

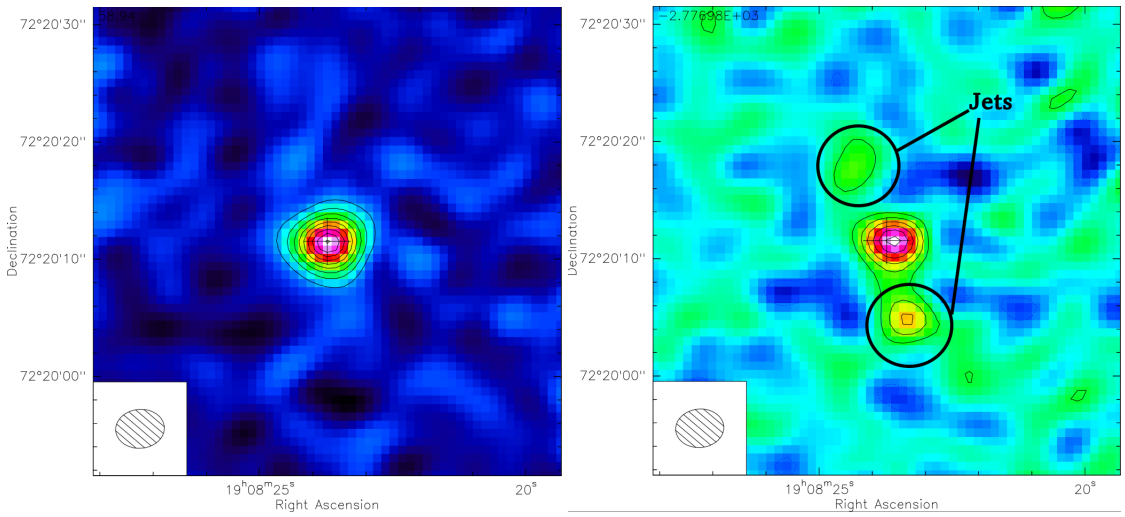

Figure 12: The image on the left shows the clean map of the CO (4-3) line emission of 6C 1909+72 with isophotal contours at -9, 9, 18, 27, ... $\times$ the local noise level. In this image, the continuum has not been subtracted, so the flux obtained by using the uv-fit command on this map is the sum of the flux of the line and the flux of the continuum. The image on the right shows the clean map of the 3-mm continuum emission from 6C 1909+72 with isophotal contours at -4, -2, 2, 6, 8, 10, 13$\times$ the local noise level. In this image, other than the emission from the centre of the galaxy, there can be seen two emission blobs above and below the galaxy, which are marked in the image. These coincide with the position of the radio jets of the galaxy. But, although the lower jet has been detected with 6σ, the upper one is only a temptative detection, with less than 3σ. At the bottom left corner of both images, the clean beam can be seen.

3 Results

3.1 Data Quality Assessement

Since the final results depend strongly on the calibration carried out, it is important to check how changing the amount of data flagged; i.e., changing the amount of data excluded from our analysis, changes the final signal-to-noise ratio (SNR) of the images. Then, after we calibrated the observations as described in Section 2.2, we obtained different maps, each of one with different visibilities flagged, by changing the quality criteria as shown in Table 1. The configuration A from this table is the one recommended by the procedure. Then, by Fourier Transforming the resulting visibilities in each case, different maps of the galaxy emission with different SNRs were obtained. Lastly, using the command "uv_fit", which fits the Fourier Transform of a point source model to the uv-table, we obtained the SNR in each case for the line and continuum emission, as seen in Table 1.

Configuration	A	B	C	D	E	F	G	H	I	J	K	L
Max. Phase RMS	40°	30°	40°	40°	40°	30°	70°	40°	40°	40°	17°	40°
Max. Amplitude loss	20%	20%	20%	10%	20%	10%	20%	40%	20%	20%	20%	20%
Max. Point corr.	30%	30%	15%	30%	30%	15%	30%	30%	50%	30%	30%	7%
Max. Focus corr.	30%	30%	30%	30%	7%	7%	30%	30%	30%	50%	30%	30%
SNR_{line}	33	33	32	33	30	30	33	33	35	33	33	29
SNR_{cont}	7	7	6	7	6	6	7	7	7	7	7	6

Table 1: Table with the parameters chosen for the Data Quality assesment. These parameters represent the maximum phase RMS, amplitude loss, point correction and focus correction that are considered acceptable, as well as the SNRs obtained for each configuration by fitting the Fourier Transform of a point source model to the visibilities obtained in each case. The maximum seeing and tracking correction established are the same for all the configurations, 1.5 arcsec and 10 % respectively. All the visibilities with higher values of these parameters are flagged.

With that, the configuration that resulted in the highest SNR was a different one than the one recommended by the procedure (configuration A shown in Figure 11a), it was the configuration I. The difference between these two configurations is that configuration I allows a larger point correction, in such a way that no visibilities were flagged due to the point correction in this case, as seen in Figure 11b. However, although configuration I provided the highest SNR, we decided against using it; since it could introduce a larger error in the position of the source by allowing a larger pointing correction.

Since the set of parameters recommended by the procedure, configuration A, gives the second higher SNR, it is the one that was used to obtain the final images. With that, the final number of scans used was 421, in contrast with the 667 scans taken during the observation; i.e. we use the 63% of the data.

3.2 Maps of the emission from 6C 1909+72

The maps of the galaxy are obtained by following the procedure explained in Section 2.2, which consists in Fourier Transforming the calibrated visibilities. In that way, a dirty map and a clean map are obtained.

In these maps, the bandwidth of 3.613 GHz centered around $\nu_{obs} = 101.721$ GHz, which corresponds to a range of velocities from -7580 to 3050 km s^{-1} and a central velocity of $V_0 = 0$, has been binned into 180 channels. To obtain maps of only the line emission or the 3-mm continuum emission, we proceed to average only the line channels and all the channel minus the ones corresponding to the line respectively. This can be done using the command "uv_average", that allows the user to select the channels to be averaged. In that way, the CO (4-3) line emission map and the continuum map presented in Figure 12 were obtained. In this figure, the maps represented are the clean maps. It is relevant to take into account that this method is not a subtraction of the continuum, therefore, the fluxes obtained from the line map will not be directly the line flux.

As a way to compare dirty and clean maps, we also present the dirty maps of the line emission in Figure 7. Here it can be seen that the effect of the beam that is present on the dirty map is mitigated in the clean map thanks to the cleaning algorithm; since the structures that can be seen in the dirty map, that are introduced by the beam, the sidelobes, are absent in the clean map. However, we only use the clean map as a visual representation of the extension of the emission, since the cleaning process introduces uncontrolled changes in the flux due to the assumption of a model of the source. Instead, to measure the flux of 6C 1909+72, we rely on the dirty map.

The continuum and line fluxes can be obtained from the clean maps using the tool "uv_fit", that fits the Fourier Transform of a point source model to the visibilities. In that way, the values shown in Table 2 were obtained. Using the line and continuum fluxes from the table, the intensity of the

line without continuum found is:

$$I_{\mathrm{CO\,(4\text{-}3)}} = (2.37 \pm 0.10)\ \mathrm{Jy\ km\ s^{-1}} \tag{3.1}$$

Parameters	Line	Continuum	Upper Jet	Lower Jet
RA	19h:08m:23.70s ± 0.06s	19h:08m:23.59s ± 0.16s	19h:08m:24.3s ± 0.6s	19h:08m:23.3s ± 0.3s
DEC	+72°:20′:11.43″ ± 0.05″	+72°:20′:11.53″ ± 0.13″	+72°:20′:18.0″ ± 0.6″	+72°:20′:04.8″ ± 0.3″
S_ν	(1.85 ± 0.06) mJy	(314 ± 28) μJy	(78 ± 28) μJy	(156 ± 28) μJy

Table 2: Table with the positions of the centres of the emission and the fluxes obtained using uv_fit.

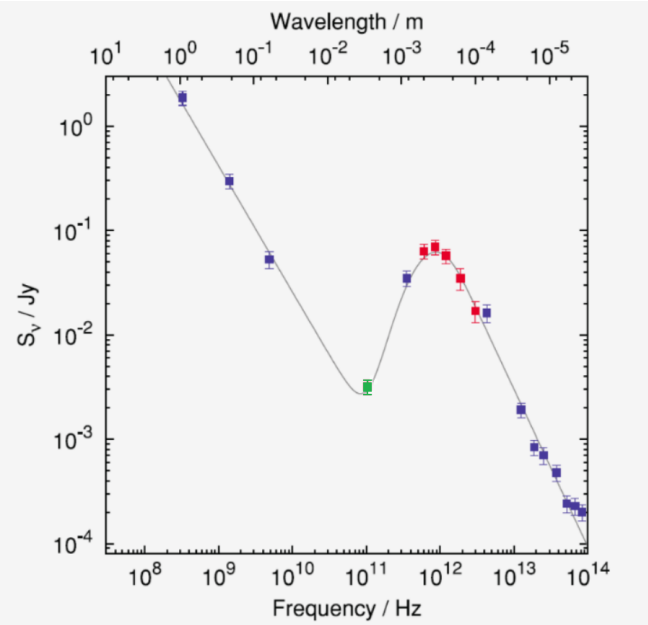

Figure 13: SED from 6C 1909+72 obtained from Ivison et al. (2012). The green point represents our continuum observation. Our result is consistent with a model of the SED that consists only in synchrotron and dust emission.

This intensity is consistent with the one found by Ivison et al. (2012), considering that they subtracted a continuum emission model from their spectra. It is important to take into account that our results present a SNR a factor 1.75 higher than previous observations of the CO (4-3) emission from 6C 1909+72, including the ones by Ivison et al. (2012).

Furthermore, as a sanity check, we represent the continuum flux from Table 2 against the SED of 6C 1909+72 from Ivison et al. (2012), as shown in Figure 13.

The model of the SED presented on Ivison et al. (2012) and shown in Figure 13 consists only on synchrotron and dust emission with a synchrotron power law index $\alpha = (-1.22 \pm 0.04)$, a power law index for the dust emission $\gamma = (5.51 \pm 0.05)$, a dust temperature $T_d = (45.7 \pm 1.3)$ K, a dust emissivity $\beta = 1.5$ and a dust mass $\log\,(M_d\,(M_\odot)) = (9.37 \pm 0.04)$. As seen in Figure 13, our data is in agreement with the dust mass and the dust temperature obtained by Ivison et al. (2012).

3.3 Is the source spatially resolved?

In order to check whether 6C 1909+72 is resolved, the amplitude is represented as a function of the baseline separation in the uv-plane as described by Geach et al. (2014). In that way, if the amplitude follows a Gaussian distribution, we can conclude that the emission is resolved (Geach et al., 2014). On the other hand, if the amplitude versus uv-radius follows a flat distribution, the emission is unresolved (Geach et al., 2014).

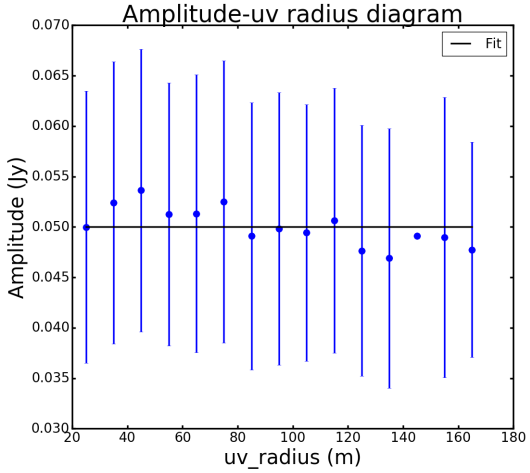

Figure 14: Amplitude vs uv-radius diagram of our observations. The data in this diagram is binned in bins of 10 m. Since the diagram is flat, we can conclude that the galaxy is not resolved.

The amplitude versus uv-radius representation can be done using the command "uvshow", from MAPPING, which represents the real part of the visibilities as a function of the Fourier Transform of the baselines; i.e., the synthesized beam. The results can be seen in Figure 14. Since the distribution of the amplitude versus the uv-radius is flat, the CO (4-3) emission from 6C 1909+72 is not spatially resolved in our observations. In that case, only an upper limit to the extension of the emission can be given, being this limit the size of the clean beam. Also, since the emission is not resolved, we cannot determine the morphology of the emission, since the morphology seen in the maps would be an effect of the beam.

The clean beam size is 4.15×3.31 arcsec^2, which is equivalent to a size of 31×25 kpc^2, using $H_0 = 71$ km s^{-1}Mpc^{-1}; $\Omega_m = 0.27$ and $\Omega_\Lambda = 0.73$. Then, the CO (4-3) extension will be < 25 kpc. Although we can only find an upper limit, this result is more restrictive than the one obtained by Papadopoulos et al. (2000) of ~ 30 kpc. In comparison, the dust emission is significantly more extended, with an extension over ~ 500 kpc according to the results of Stevens et al. (2003).

3.4 Motion of the molecular gas

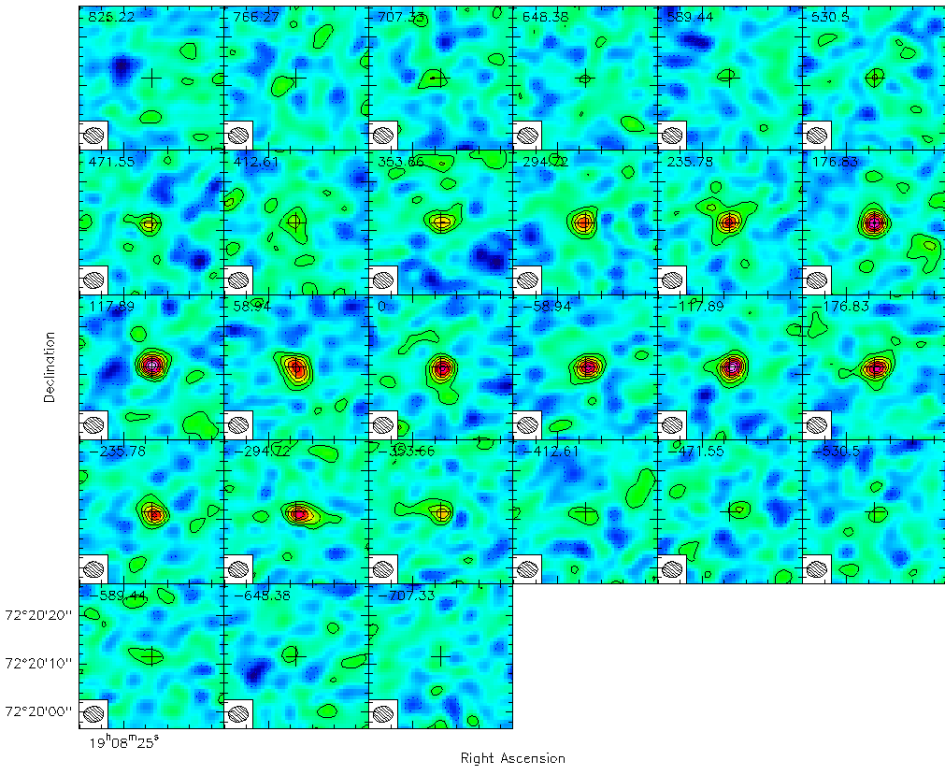

Figure 15: This figure shows the channel maps of the galaxy from a velocity of -707.33 km s^{-1} to a velocity of 825.22 km s^{-1} in steps of 60 km s^{-1} (our channel width). Since the CO (4-3) emission is centered around the same region in all the channels, we can conclude that we cannot observe any gradients of the molecular gas in the galaxy.

The presence of velocity gradients of the molecular gas inside the galaxy could indicate that the galaxy presents motion of the gas, such as molecular gas outflows or inflows or that the galaxy is undergoing a merger stage, depending on the properties of these gradients. Therefore, checking the existence of velocity gradients could give a better understanding of the physical processes that may be responsible for the extended dust emission.

To check whether there are velocity gradients of the molecular gas inside the galaxy, the channel maps are created. These maps (Figure 15) show the CO (4-3) emission from an individual channel; i.e., the CO (4-3) emission is shown in bins of 60 km s^{-1}. In that way, if the emission is centered around different regions in consecutive channel maps, we can conclude that the CO gas in the galaxy presents velocity gradients.

In the case of 6C 1909+72, the emission of the CO (4-3) line is centered around the same region in all the channel maps. Then, we conclude that no velocity gradients of the molecular gas can be observed with our channel width of 60 km s^{-1}.

3.5 CO (4-3) line properties

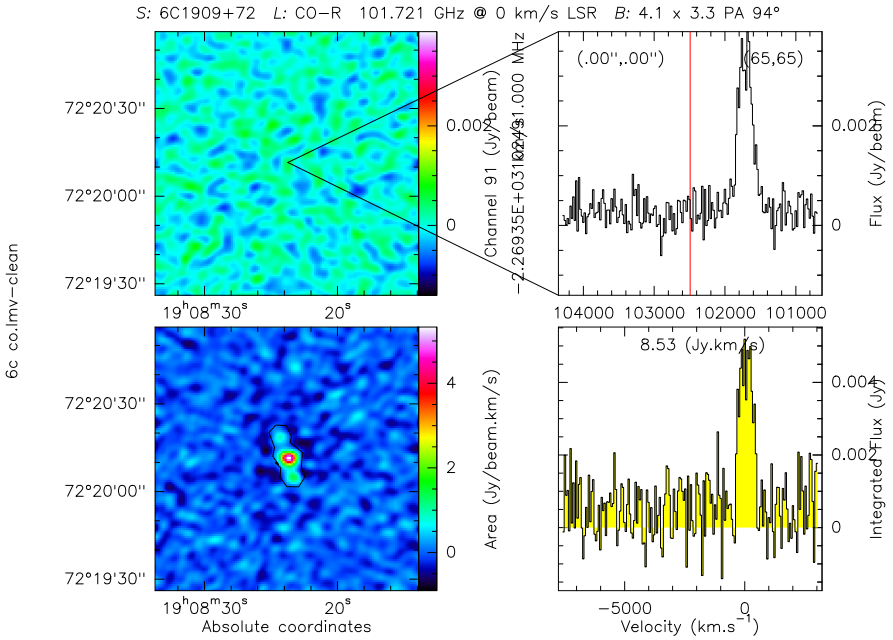

Figure 16: Maps of 6C 1909+72 with the line and continuum emission as seen with the interactive tool "go view" from MAPPING are shown. The squares above represent the emission at the selected channel (on the left), in this case the 91^{st} channel, and the spectrum of the same channel (on the right). The squares below represent the uv-map obtained by averaging all the channels (on the left) and the integrated spectrum from the region selected using the polygon (on the right).

To obtain the spectrum of 6C 1909+72 centered around the CO (4-3) line, we extracted it from the dirty map using two different methods. It is important to point out that we used the dirty map instead of the clean map since the fluxes from the clean map could be modified by the cleaning algorithm. The two methods for extracting the spectrum of the galaxy are the following:

- The first method is the one that is usually carried out for NOEMA observations and consists on selecting a polygon that contains all the emission from the galaxy using the interactive tool "go view" from MAPPING. The spectrum corresponding to the integrated flux inside the region selected with the polygon can be seen at the bottom right corner of Figure 16. This spectrum can be then obtained as an ASCII table. With this method, we obtained the spectrum that can be seen in Figure 17a. However, since we have to select a polygon manually and the limit of the emission is influenced by the color representation of the map, the spectrum is affected by the way the polygon is chosen, hence the use of the second method. For instance, the flux of the line for the polygon selected was 1.3 times the flux of the line obtained with the second method; while the FWHM of the line was 0.8 times the one obtained with the second method.

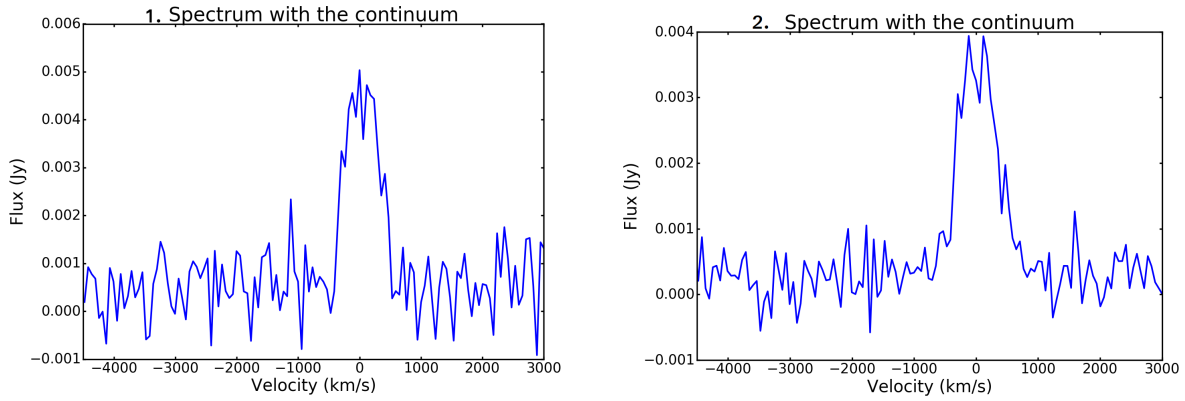

(a) (b)

Figure 17: Figure a shows the spectrum obtained using the first method (the polygon method), including continuum, can be seen. Figure b shows the spectrum of the galaxy obtained using uv_fit, including continuum. The line observed is the emission line from the CO (4-3) transition.

- For the second method, the flux from every channel is obtained using the command "uv_fit"; in such a way that a table can be written with the results of fitting the Fourier Transform of a point source model to each channel. The spectrum obtained using this method can be seen in Figure 17b. Since the first method depends on the polygon selected, we will use the spectrum obtained using this last method to carry out our analysis.

3.5.1 Gaussian fit

To study the galaxy CO (4-3) emission, first, it is necessary to subtract the continuum emission from the line emission. To do that, a first-degree polynomial was fitted to the continuum emission and, then, it was subtracted from the spectrum (Figure 17b). In the spectrum obtained (Fig. 18), it can be observed that the CO (4-3) line presents a double horn profile that could be indicative of the existence of two unresolved CO (4-3) lines.

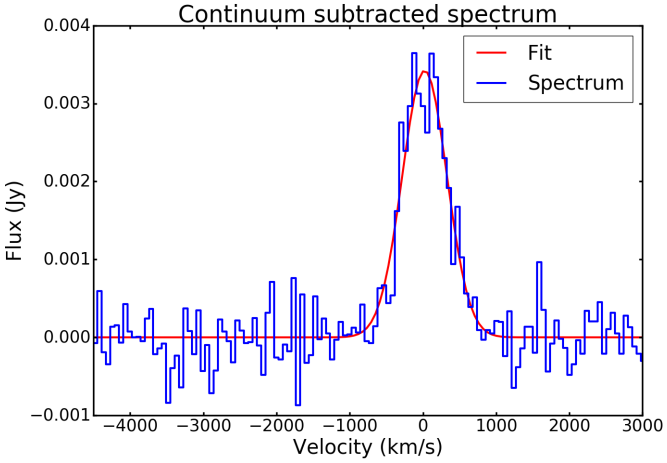

Figure 18: Gaussian fit to the continuum subtracted spectrum. The properties of the emission can be derived from the properties of the resulting Gaussian, that can be seen on Table 3.

Once the continuum-free spectrum is obtained, we proceed to fit a Gaussian profile to the CO (4-3) line. The results of that fit can be seen in Figure 18.

With that, we can conclude that the CO (4-3) emission has the properties shown in Table 3, which are consistent with the results from Ivison et al. (2012), but with a better SNR.

V_0 (km s^{-1})	23 ± 13
S_ν (mJy)	3.42 ± 0.13
FWHM (km s^{-1})	718 ± 31
$I_{\mathrm{CO\ (4\text{-}3)}}$ (Jy km s^{-1})	2.62 ± 0.15

Table 3: Properties of the CO (4-3) line obtained using the Gaussian fit. These are the central velocity of the line, V_0, the flux from the line, S_ν, its full-width at half maximum, FWHM, and the intensity of the line, $I_{\mathrm{CO\ (4\text{-}3)}}$. These properties are consistent with the results from Ivison et al. (2012).

To obtain the redshift of 6C 1909+72 from the CO (4-3) observations, we need to establish a transformation between velocity and frequency, since the spectrum is obtained as a function of the gas velocity. This transformation has the following form:

$$\nu = -\frac{ch_\nu}{ch_c} \cdot V + \nu_0 \tag{3.2}$$

where ν is the frequency, V is the velocity, ch_ν is the channel width in frequency, ch_c is the channel width in velocity and ν_0 is the central frequency of the observations, in our case, $\nu_0 = 101.721$ GHz. Therefore, to obtain the transformation from velocity to frequency, the channel widths in frequency and in velocity have to be known.

Knowing that our observations have 180 channels and a bandwidth of 3600 MHz, the channel width in frequency is $ch_\nu \simeq 20$ MHz. Then, taking into account that the resolution computed using the velocity channel width has to be the same as if it is computed using the frequency channel width; i.e.:

$$R = \frac{\nu_0}{ch_\nu} = \frac{c}{ch_c} \tag{3.3}$$

where R is the resolution and c is the velocity of the light; the channel width in velocity units is $ch_c \simeq 60$ km s^{-1}. With that, using equation (3.2), the transformation from velocity to frequency is:

$$\nu = -0.34 \left(\mathrm{MHz}\ \left(\mathrm{km\ s^{-1}}\right)^{-1}\right) V + 101721\ \mathrm{MHz} \tag{3.4}$$

Using this equation, the central frequency of the line can be obtained from the central velocity shown in Table 3:

$$\nu_{\mathrm{CO\ (4\text{-}3)}} = (101713 \pm 5)\ \mathrm{MHz} \tag{3.5}$$

and the redshift of the line is:

$$z_{\mathrm{CO\ (4\text{-}3)}} = (3.5328 \pm 0.0002) \tag{3.6}$$

This result is consistent with the redshift of 6C 1909+72 found by Ivison et al. (2012) and Papadopoulos et al. (2000) for the same transition, but with a much lower error, as it can be seen in Figure 19.

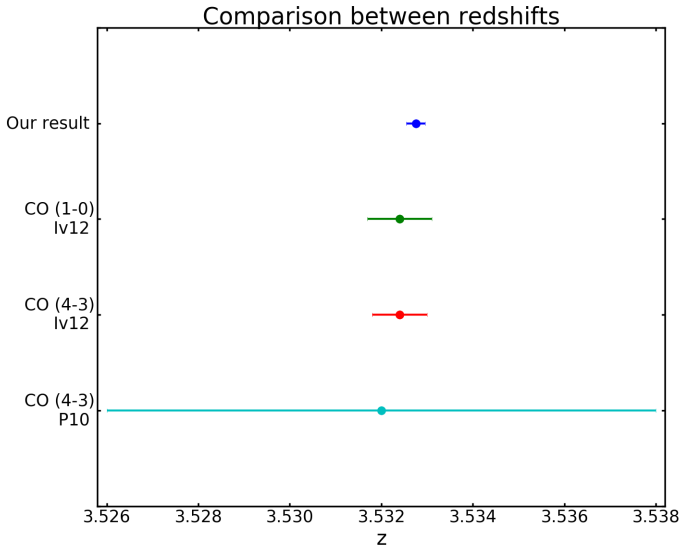

Figure 19: Comparison between the redshifts of the CO (4-3) line from this work, Ivison et al. (2012) (Iv12) and Papadopoulos et al. (2010) (P10), and the redshift of the CO (1-0) line from Ivison et al. (2012). Our result is consistent with the results obtained by other authors but with significantly less error.

3.5.2 Molecular outflows

One of the possible explanations of the extended dust emission from 6C 909+72 found by Stevens et al. (2003) is that the galaxy presents metal-rich gas and dust entrained collimated outflows. To check the existence of these outflows, we use the criteria described by Cicone et al. (2013). According to this criteria, to conclude that a galaxy presents molecular outflows, at least two of the following conditions have to be verified:

- The CO emission FWHM has to be larger than 500 km s^{-1}.
- The CO line has to present broad CO wings of, at least, 300 km s^{-1}.
- Molecular profiles have to have been already detected through P-Cygni profiles.

To determine whether the CO (4-3) line emitted by 6C 1909+72 presents wings, the base of the line is shown in Figure 20. Since no significant wings can be observed, the FWHM of the line is $\sim$ 700 km s^{-1} and no velocity gradients were found using the channel maps; we can conclude that 6C 1909+72 presents no significant molecular outflows. In that case, there are only two possible explanations left for the extended dust morphologies: that the emission actually comes from two galaxies in the line-of-sight, i.e., line-of-sight blends; or that 6C 1909+72 is undergoing a merging process of two or more components.

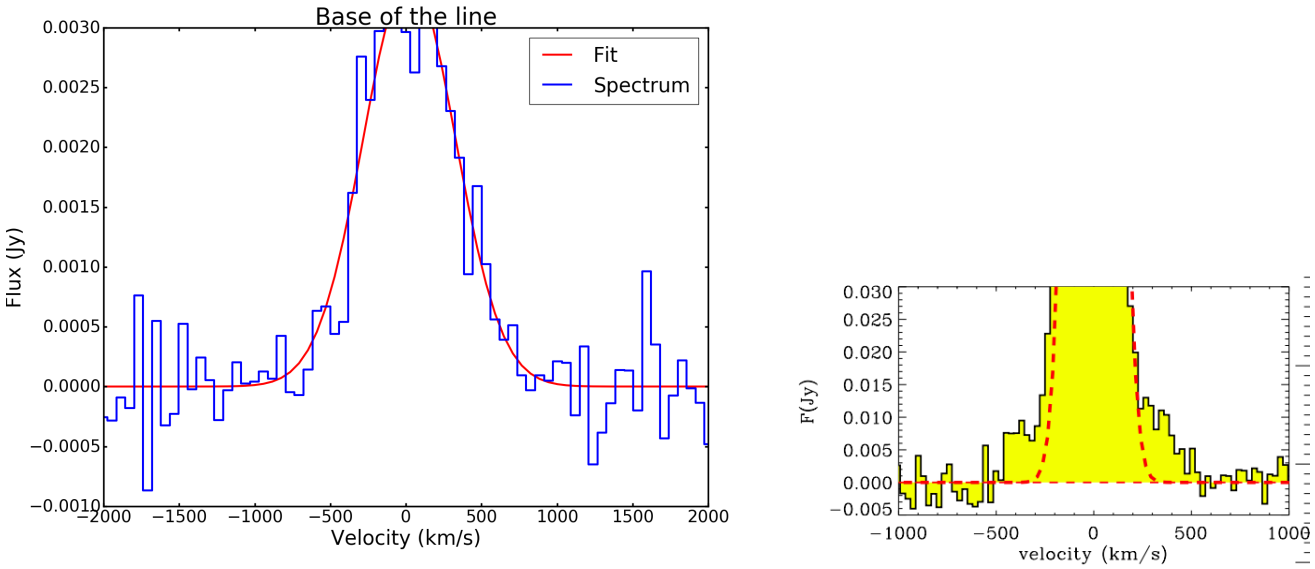

Figure 20: The figure on the left represents a zoom to the base of the line where no wings can be seen. The figure on the right is a spectrum of a line with broad wings obtained by Cicone et al. (2014) that is shown as a way to compare a line with and without wings.

3.5.3 Galaxy components

Although the line-of-sight blends explanation is the less likely, since, according to blank-field surveys, we should find on average one submillimeter source per SCUBA at $S_{850} > 5-6$ mJy (Stevens et al., 2003); it cannot be entirely ruled out. Then, to discern between the line-of-sight blends and the merger scenarios, the CO (4-3) line was fitted using a two Gaussian model that could reproduce a single Gaussian fit.

Since there is not a unique combination of two Gaussians that can reproduce the single Gaussian fit; we program a local search algorithm. This algorithm allows finding the optimal values of a set of free parameters using a function that gives information about the goodness of the parameters. This function is usually known as the "evaluation function". Our set of free-parameters consists on the parameters of the two Gaussians and the evaluation function compares the sum of the two Gaussians with both, the single Gaussian fit and our data. Some of the most representative solutions obtained can be seen in Figure 21 and in Table 4.

According to our results, the line emission could be due to the emission of two components, but also, to the emission of a single component. These two components would emit CO (4-3) lines with similar FWHMs, that range from 450 to 700 km s^{-1}, which are typical values for SMGs, as found by Bothwell et al. (2013). In this case, the extended dust morphologies would be the result of the merge of these two components. However, the explanation of the line-of-sight blend cannot be entirely ruled out, since the two assumed lines are not resolved and the observed line can also be fitted using a single Gaussian (Figure 18).

Fits	S_ν^1 (mJy)	S_ν^2 (mJy)	V_0^1 (km s^{-1})	V_0^2 (km s^{-1})	FWHM^1 (km s^{-1})	FWHM^2 (km s^{-1})
Fit 1	2.6	2.1	-133	225	533	508
Fit 2	2.1	1.3	9	44	705	736
Fit 3	2.2	2.6	-181	181	485	534
Fit 4	1.3	2.3	-120	102	654	676

Table 4: In this table, some of the most significant results from the local search are shown. The parameters shown are the fluxes, S_ν^i, the central velocities, V_0^i, and the full-widths at half maximum, FWHM^i, of the line for both components obtained from the Gaussian fit.

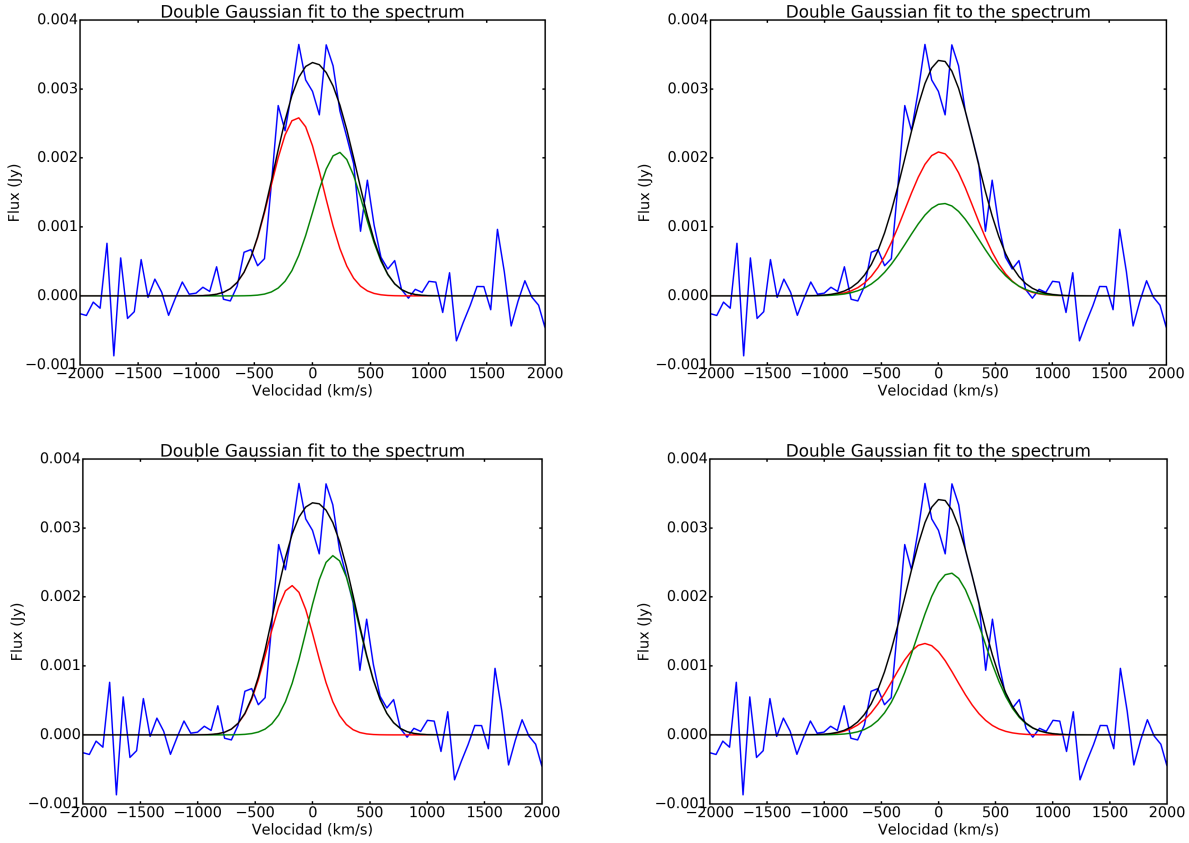

Figure 21: Possible different components that recreate the single Gaussian fit to the CO (4-3) line. The single Gaussian fit can be recreated as the sum of two Gaussian components with similar FWHMs that go 450 from to 700 km s^{-1}, which are typical values for SMGs as found by Bothwell et al. (2013). However, we cannot conclude that the line emission is actually due to two components, since the two alleged lines are not resolved.

4 Discussion

4.1 Possible scenarios

With the results obtained, we can achieve the main goal of this work: to distinguish among the three possible scenarios that could explain the extended submillimeter emission from 6C 1909+72 as well as from other HzRGs detected by Stevens et al. (2003), which are:

1. Line-of-sight blends, i.e., the emission observed from 6C 1909+72 is the joint emission from it and another galaxy superimposed in the line of sight. In this case, the emission from the CO (4-3) transition can be modeled using only a narrow Gaussian profile.

2. Gas-rich mergers. In this scenario, the extended emission is caused by the merging of two or more components. Then, with enough spectral resolution, the different CO (4-3) lines for each component can be resolved and the CO (4-3) line can be modeled using two or more narrow Gaussian profiles.

3. Metal-rich gas and dust entrained in collimated outflows. This last scenario is verified if the CO (4-3) line can be fitted using a broad Gaussian line and if it presents broad emission wings.

In the first two scenarios, the FWHM of the line expected would be $\sim$ 500 km s^{-1} and the peak flux density of the line would be $S_\nu \sim 2.1$ mJy. On the other hand, in the outflow scenario, we would expect a FWHM$\sim$ 1000 km s^{-1} and half the peak flux density of the line than in the other scenarios.

We do not observe any motion of the gas and the CO (4-3) line does not present broad wings and can be fitted using a narrow Gaussian. Furthermore, from the Gaussian fit, we obtain a FWHM of the line $\sim$ 700 km s^{-1} and a peak flux density of the line $\sim$ 3.4 mJy. Then, following the criteria described by Cicone et al. (2013), we can conclude that there are no molecular gas outflows in 6C 1909+72, excluding the third scenario for the origin of the extended submillimeter emission.

The only possible scenarios left are the line-of-sight blends scenario and the merger scenario and, although the line-of-sight blend scenario is the less likely, it cannot be entirely ruled out since we do not observe any velocity gradients of the gas in the channel maps that could imply the presence of different components. Furthermore, the CO (4-3) line can be fitted using a single narrow Gaussian profile, in such a way that, if there were several components in the galaxy, their corresponding CO (4-3) lines would be unresolved.

To discern between these two scenarios we study the possible ways in which the single Gaussian profile could be reproduced using the sum of two Gaussians; i.e., we study the possibility of the galaxy being formed by two unresolved components. In that way, we find that the CO (4-3) line from 6C 1909+72 can be explained by a model of two unresolved narrow lines with similar properties. These lines would have FWHMs ranging from $\sim$450 to 700 km s^{-1}, typical values for Submillimeter Galaxies (SMGs). However, since there is not a unique combination of the two components and since the single Gaussian model provides also a good fit to the line profile, we cannot exclude either of the scenarios. In order to discriminate between them, observations with better spectral resolution would be required in order to resolve the CO (4-3) lines from the alleged components.

4.2 Brightness Temperature Ratio

The low-J transitions of CO are the most appropriate to trace the diffuse molecular gas (Section 1.2.2). In particular, the CO (1-0) transition provides the best tracer for this diffuse gas, since higher transitions could missed part of the colder gas (Bothwell et al., 2013). That is why it is important to establish a conversion factor between the emission of a CO (J+1-J) transition and the CO (1-0) transition. This conversion factor is known as the brightness temperature ratio, $r_{J+1-J/1-0}$, and can be written as:

$$r_{J+1-J/1-0} = \frac{L'_{\text{CO (J+1-J)}}}{L'_{\text{CO (1-0)}}} = \frac{I_{\text{CO (J+1-J)}}\nu^2_{\text{CO (1-0)}}}{I_{\text{CO (1-0)}}\nu^2_{\text{CO (J+1-J)}}} \tag{4.1}$$

The values of the ratios usually taken are the ones presented by Bothwell et al. (2013). They presented the results of a survey of CO observations for SMGs, in particular, they observed the CO (4-3) emission from 6 SMGs and they used the CO (1-0) transition information available from the literature. In that way, they obtained $r^{Bothwell}_{4-3/1-0} = (0.41 \pm 0.07)$ for high-redshift starbursts. However, Ivison et al. (2012) carried out observations of the CO (1-0) and the CO (4-3) transitions of 6C 1909+72 and found a brightness temperature ratio $r^{Ivison}_{4-3/1-0} = (0.76 \pm 0.18)$. Some other works (e.g. Emonts et al., 2018) also found discrepancies with the value given by Bothwell et al. (2013), finding a value closer to one, as seen in Table 5. A value closer to one implies that the molecular gas is thermalized and that it is optically thick up to $J = 4$ (Solomon & Vanden Bout, 2005 and Aravena et al., 2010), since the emission from the different transitions would be the same (Carilli & Walter, 2013). This could be due to the existence of a source of heating of the gas in HzRGs that is not present in SMGs, which could be the AGN or the radio jets (Ivison et al., 2012).

In order to find out which value of the brightness temperature ratio provides the most consistent results, we used both to obtain the CO (1-0) luminosity and the gas mass, as well as to transform the equations from the literature shown in section 4.3. We also obtained $r_{4-3/1-0}$ taking the CO

(1-0) line intensity from Ivison et al. (2012), $I_{\mathrm{CO\,(1\text{-}0)}}$ =(0.222 $\pm$ 0.049) Jy km s^{-1}, finding:

$$r_{4-3/1-0} = (0.74 \pm 0.17) \tag{4.2}$$

which is consistent with the result obtained by Ivison et al. (2012). However, this result was obtained using their CO (1-0) line intensity, so it does not constitute an independent check, although the CO (4-3) line intensity value used was the one obtained from our observations.

To find out whether the brightness temperature ratio changes from a galaxy to another even if they are both HzRGs and whether the value from Bothwell et al. (2013) is actually correct; we computed $r_{4-3/1-0}$ for different HzRGs using line intensity values gathered from the literature. The values obtained can be seen in Table 5.

In that way, if we only considered the values of the brightness temperature ratio of the galaxies with $I_{\mathrm{CO\,(1\text{-}0)}}$ and $I_{\mathrm{CO\,(4\text{-}3)}}$ (since the ratios obtained using the luminosities depend on the cosmology chosen by the authors), all of the values of $r_{4-3/1-0}$ are higher than the one obtained by Bothwell et al. (2013) for SMGs; being in most cases near to one. This means that the molecular gas in HzRGs is thermalized while in SMGs it is sub-thermalized; laying bare the presence of an additional source of gas heating in HzRGs that does not exist in SMGs. Moreover, there is not a unique value that can be considered acceptable for all the HzRGs, since the values of $r_{4-3/1-0}$ range from $\sim$0.7 up to $\sim$2. This diversity in the $r_{4-3/1-0}$ for HzRGs could be due to differences in the environments of the molecular gas among the HzRGs.

To get to understand the behavior of the brightness temperature ratio in different HzRGs, more observations of different CO transitions for the same galaxies are needed. However, we can conclude that there is not a unique value applicable to all HzRGs and that using an incorrect value of the brightness temperature ratio can lead to a significant overestimation up to a factor 2 in the values of the gas mass of the galaxies.

4.3 Comparison of different high-redshift galaxies

Using our results, we can derive the main properties of 6C 1909+72 in order to be able to compare it with other HzRGs, as well as to the SMGs with CO (4-3) observations from Bothwell et al. (2013) and the quasars (QSOs) with CO (4-3) observations from Carilli & Walter (2013). We choose to compare HzRGs to SMGs and QSOs since all of these kinds of galaxies are starbursts at high-redshifts, so we expect them to have similar properties.

Here, we present a compilation of different HzRGs (Table 5). The sample of galaxies of the compilation are HzRGs for which observations of the CO (4-3) line have been obtained. These galaxies have redshifts from 2 to 4, molecular masses in the range of $\sim 10^{10} - 10^{11}$ M$_\odot$ and stellar masses around $\sim 10^{10} - 10^{12}$ M$_\odot$. For most of these galaxies, there are not CO (1-0) observations. This is because synchrotron emission dominates at $\sim$ 115 GHz, which is the central frequency of the CO (1-0) line, complicating the CO (1-0) observations for HzRGs.

The fluxes of 6C 1909+72 at different wavelengths as well as the different properties of the galaxy can be seen in Tables 6 and 7. The properties compiled on these tables were obtained from the literature as well as based on our CO (4-3) data.

The CO luminosities shown in Tables 5 and 7 , $L'_{\mathrm{CO\,(4\text{-}3)}}$ and $L'_{\mathrm{CO\,(1\text{-}0)}}$, were obtained using the expresion from Walter et al. (2003):

$$L'_{\mathrm{CO\,(J+1,\,J)}} = 3.25 \cdot 10^7 \cdot S_{\mathrm{CO\,(J+1,\,J)}}\Delta\nu \cdot \nu_{obs}^{-2} \cdot D_L^2 \cdot \left(1 + z_{\mathrm{CO\,(J+1,\,J)}}\right)^{-3} \tag{4.3}$$

where $S_{\mathrm{CO\,(J+1,\,J)}}\Delta\nu$ is the integrated flux density; i.e, the line intensity in Jy km s^{-1}; ν_{obs} is the observing frequency in GHz; D_L is the luminosity distance in Mpc; and $z_{\mathrm{CO\,(J+1,\,J)}}$ is the redshift of the CO (J+1, J) transition. To compute the luminosities, we took: H_0 = 71 km s^{-1}Mpc^{-1}; $\Omega_m = 0.27$ and $\Omega_\Lambda = 0.73$. This is the cosmology chosen by Ivison et al. (2012) and by Bothwell et al. (2013) in order to facilitate the comparison of the results.

The way of obtaining the brightness temperature ratio, $r_{4-3/1-0}$, is explained in the previous section.

The CO (1-0) luminosity and the properties related to it shown in Tables 5 and 7 are computed using both brightness temperature ratios, the one obtained by Bothwell et al. (2013) for SMGs and the one obtained by Ivison et al. (2012) for 6C 1909+72. The gas mass was obtained using the CO (1-0) luminosity to gas mass ratio presented in Downes & Solomon (1998) for starburst galaxies: $\alpha_{\mathrm{CO}} = 0.8\ M_{\odot} \left(\mathrm{K\ km\ s^{-1}\ pc^2}\right)^{-1}$. Lastly, the molecular gas fraction, f_{mol}, is defined as: $f_{mol} = \frac{M_{mol}}{M_* + M_{mol}}$ and was computed using the brightness temperature ratio from Ivison et al. (2012) and the stellar mass from Smith et al. (2010).

To compare 6C 199+72 to other high-redshift starbursts and, also, to determine whether the properties of the galaxy obtained in this work are in accordance with the models and the observations presented for high-redshift galaxies in Sargent et al. (2014) and in Bothwell et al. (2013); we represent plots from Figures 22a, 22b and 23.

4.3.1 Schmidt-Kennicutt plot: star-formation law

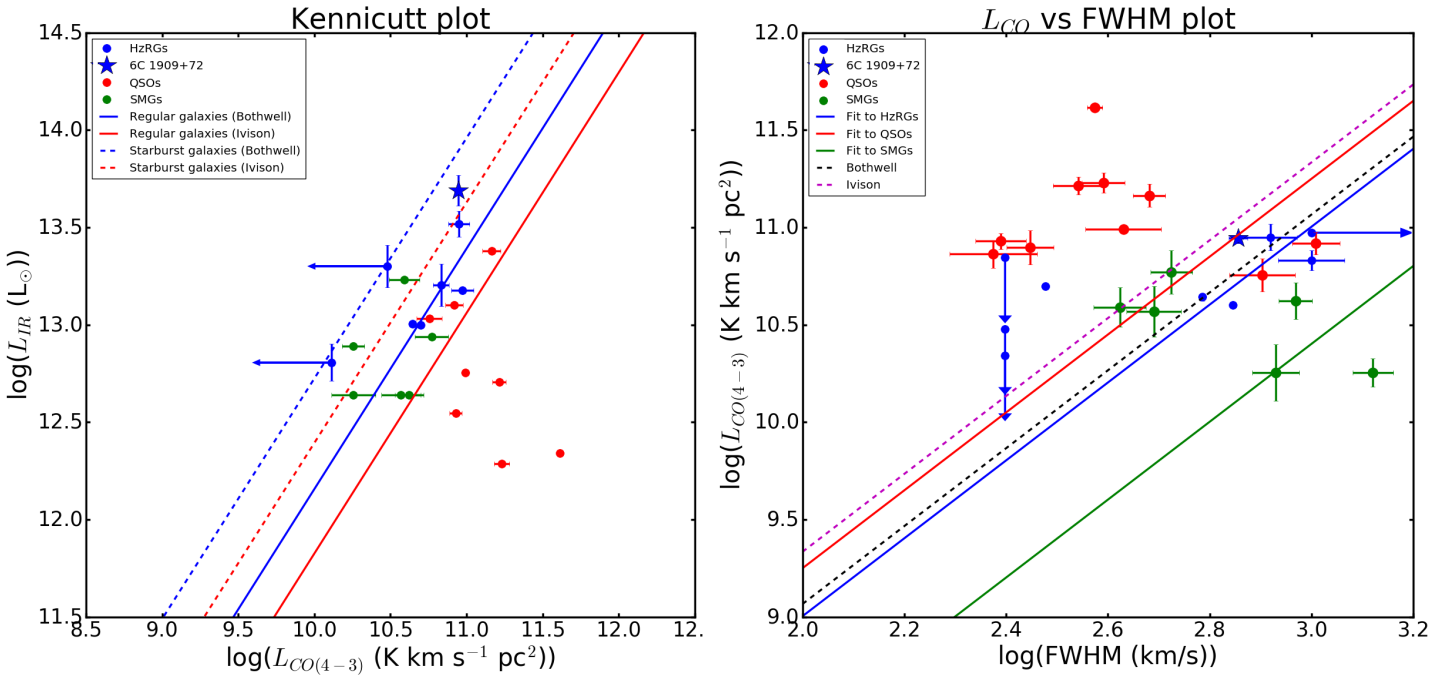

(a) (b)

Figure 22: Plots comparing the properties of different HzRGs, SMGs and QSOs. (a): Kennicut plot. In this plot, the infrared luminosity, L_{IR}, is represented as a function of the CO (4-3) luminosity, $L'_{\text{CO (4-3)}}$. The galaxies represented are HzRGs, SMGs, and QSOs as blue, green and red dots. The blue star corresponds to 6C 1909+72. The lines represent the Kennicutt law for starburst galaxies (dashed lines) and for normal galaxies (solid lines) using the brightness temperature ratios from Bothwell et al. (2013) and Ivison et al. (2012). (b): In this plot, the luminosity of the CO (4-3) line, $L'_{\text{CO (4-3)}}$, is represented as a function of the FWHM of the line. The blue, green and red dots represent HzRGs, SMGs, and QSOs respectively. 6C 1909+72 is represented as a blue star. The dashed lines represent the model from Bothwell et al. (2013) using the temperature brightness ratios from Bothwell et al. (2013) and Ivison et al. (2012); while the solid lines represent the fits to the function from Bothwell et al. (2013) to the different types of galaxies (HzRGs, SMGs and QSOs).

The Schmidt-Kennicutt law represents the empirical relation of the star-formation rate (SFR) with the molecular gas mass, M_{gas}, of a galaxy (see Section 1.2.2). Since the SFR and the M_{gas} are related to the infrared luminosity, L_{IR}, and to the CO (1-0) luminosity, $L'_{\text{CO (1-0)}}$ respectively, these two magnitudes can also be related using the Schmidt-Kennicutt law. Establishing this empirical relationship for HzRGs and other high-z starbursts provides a better understanding on how efficiently these galaxies transform their gas content into stars. In that way, the Schmidt-Kennicutt plot (Figure 22a) represents the infrared luminosity as a function of the CO luminosity. The galaxies represented in this plot are the HzRGs from Table 5, the SMGs with CO (4-3) observations from Bothwell et al. (2013) and the QSOs with CO (4-3) observations from Carilli & Walter (2013).

The law that the galaxies are expected to follow is the one presented in Sargent et al. (2014). However, this expresion represents the CO (1-0) luminosity as a function of the infrared luminosity; so, to be able to apply this expression to our data, we need to rely on the brightness temperature ratio.

In that way, the resulting expressions are the following:

$$\text{Using } r_{4-3/1-0}^{Bothwell}\text{: } \begin{cases} \log\left(L'_{\text{CO (4-3)}}\right) = (0.15 \pm 0.09) + (0.81 \pm 0.03)\log\left(L_{IR}\right) & \text{regular galaxies} \\ \log\left(L'_{\text{CO (4-3)}}\right) = \left(-0.31\,^{+0.22}_{-0.15}\right) + (0.81 \pm 0.03)\log\left(L_{IR}\right) & \text{starbursts} \end{cases} \tag{4.4}$$

$$\text{Using } r_{4-3/1-0}^{Ivison}\text{: } \begin{cases} \log\left(L'_{\text{CO (4-3)}}\right) = (0.42 \pm 0.12) + (0.81 \pm 0.03)\log\left(L_{IR}\right) & \text{for regular galaxies} \\ \log\left(L'_{\text{CO (4-3)}}\right) = \left(-0.04\,^{+0.27}_{-0.20}\right) + (0.81 \pm 0.03)\log\left(L_{IR}\right) & \text{for starbursts} \end{cases} \tag{4.5}$$

We expect the value of $r_{4-3/1-0}$ obtained by Bothwell et al. (2013) to provide a Schmidt-Kennicutt law typical for SMGs since this is the kind of galaxies they used to obtain their brightness temperature ratios; while the ratio obtained by Ivison et al. (2012) would provide a law more appropriate for HzRGs, that seem to have brightness temperature ratios closer to 1, in general, than SMGs.

Since the galaxies represented are all starbursts, it would be expected that they followed either of the Kennicutt laws for starburst galaxies. However, since our sample contains only 7 galaxies of each type and due to the dispersion of the data, we cannot claim that they follow neither of the laws presented in specific.

On the other hand, while, both, HzRGs and SMGs follow the same Kennicutt-Schmidtlaw, the QSOs form a cloud in the diagram. This could be explained by taking into account that QSOs are much more excited systems than SMGs (Carilli & Walter, 2013), which means that their brightness temperature ratio has to be larger than the one for SMGs. In that way, the Schimidt-Kennicutt relation for QSOs would be moved towards lower infrared luminosities. However, due to the small amount of data in our sample, we cannot get to a conclusion on the parameters of this relation.

4.3.2 Relation of the luminosity and the FWHM of the line

According to Botwell et al. (2013), there is a relation between the luminosity of the CO (1-0) line and its FWHM, which trace the molecular gas mass and the dynamics of the potential well where the gas lies. This relation can be considered a "Tuly-Fisher-like relation". The baryonic Tuly-Fisher relation is the relation between the angular momentum and the dynamical mass of disk galaxies that appears when the fraction of the angular momentum and mass of the baryons is a constant fraction of the relation between the angular momentum and mass of the dark matter halo (Dannerbauer et al., 2017).

Bothwell et al. (2013) interpreted this relation as the existence of a uniform ratio of the gas-to-stellar contribution to the dynamics of the potential well. However, this relation is expected to have some dispersion due to the fact that the FWHM is sensitive to the inclination. The relation shown in Bothwell et al. (2013) is the following:

$$L'_{\text{CO (1-0)}} = \frac{C\left(\text{FWHM}/2.35\right)^2}{2 \cdot 1.36 \alpha_{\text{CO}} G} R \tag{4.6}$$

where C is a constant parameterizing the kinematics of the galaxy ($C = 2.1$ for a disk galaxy according to Erb et al., 2006); α_{CO} is the CO (1-0) luminosity to gas mass conversion factor ($\alpha_{\text{CO}} = 0.8\ \text{M}_\odot \left(\text{K km s}^{-1}\ \text{pc}^2\right)^{-1}$ for starbursts galaxies according to Downes & Solomon, 1998); G is the gravitational constant in astronomical units ($G = 4.302 \cdot 10^{-3}\ \text{pc M}_\odot^{-1}\text{km}^2\text{s}^{-2}$); and R is the radius of the CO (1-0) emission region, which is usually considered $R \sim 7$ kpc for SMGs (Ivison et al., 2011). The factor 2 in the equation was added a posteriori (Dannerbauer, personal communication, 2018) since it was missing from the original equation in Bothwell et al. (2013).

In that way, we intend to determine whether this relation is maintained for the CO (4-3) transition. Then, we can represent $L'_{\text{CO (4-3)}}$ as a function of the FWHM using the brightness temperature ratio as shown in Figure 22b for the HzRGs from Table 5, as well as the SMGs from Bothwell et al. (2013)

and the QSOs from Carilli & Walter (2013).

Apart from representing the equation (4.6) using the brightness temperature ratios presented in Bothwell et al. (2013) and in Ivison et al. (2012); we fitted the different sets of values using:

$$L'_{\mathrm{CO\,(4\text{-}3)}} = a \cdot \mathrm{FWHM}^2 \tag{4.7}$$

According to the plot, the CO (4-3) luminosity does not seem to follow the same relation with the FWHM of the CO (4-3) line as the CO (1-0) emission does. Even so, this effect could be only due to the little amount of observations in our sample. On the other hand, the lack of correlation between these two magnitudes could be explained by the combined effect of the galaxies gas reservoirs having different geometries and a higher contribution of the stellar mass in the potential well in some of the galaxies as suggested by Bothwell et al. (2013) for $z \sim 0$ Ultra Luminous Infrared Galaxies.

Another possible explanation why the $L'_{\mathrm{CO\,(4\text{-}3)}}$ does not follow the same relation with the FWHM as the $L'_{\mathrm{CO\,(1\text{-}0)}}$ is the fact that higher J transitions of the CO trace denser and more centrally concentrated molecular gas, so using the same radius, R, for the relation of the luminosity of the CO (4-3) transition than for the one of the CO (1-0) transition could lead to an incorrect value of the slope of the relation.

4.3.3 Molecular gas fraction vs. stellar mass

Sargent et al. (2014) presented a model for the evolution of the molecular gas fraction with the stellar mass according to the redshift of the galaxies. According to this model, the molecular gas fraction of a main sequence galaxy can be written as:

$$f_{mol} = \frac{1}{1 + \frac{M_*^{1-\beta}}{D} \cdot \mathrm{sSFR}^{-\beta}} \tag{4.8}$$

where $D = 10^{\alpha}$, M_* is the stellar mass and sSFR is the specific star formation rate, that can be parametrized as:

$$\mathrm{sSFR}\,(M_*,\, z) = N\,(M_*)\, \mathrm{e}^{\frac{Az}{1+Bz^C}}$$

being $N\,(M_*) = N\left(5 \cdot 10^{10}\,\mathrm{M}_\odot\right) 10^{\nu \log\left(M_*/5\cdot 10^{10}\,\mathrm{M}_\odot\right)}$, where ν is the slope of the $\log(\mathrm{sSFR})$ versus $\log(M_*)$ relation and $N\left(5 \cdot 10^{10}\,\mathrm{M}_\odot\right)$ is the normalization factor at a stellar mass of $5 \cdot 10^{10}\,\mathrm{M}_\odot$. The parameters presented in Sargent et al. (2014) are the following:

$$\begin{cases} A = \left(2.05\,^{+0.33}_{-0.20}\right) \\ B = \left(0.16\,^{+0.15}_{-0.07}\right) \\ C = (1.54 \pm 0.32) \end{cases} \qquad \begin{cases} \nu = (-0.21 \pm 0.04) \\ N\left(5 \cdot 10^{10}\,\mathrm{M}_\odot\right) = \left(0.095\,^{+0.002}_{-0.003}\right)\ \mathrm{Gyr}^{-1} \end{cases}$$

For normal galaxies: $\begin{cases} \alpha = (9.22 \pm 0.02) \\ \beta = (0.81 \pm 0.03) \end{cases}$ For starburst galaxies: $\begin{cases} \alpha = \left(8.05\,^{+0.29}_{-0.10}\right) \\ \beta = (0.81 \pm 0.03) \end{cases}$

Using this model, we present a plot (Figure 23) in which the evolution of the molecular gas fraction with the stellar mass is shown for normal and starburst galaxies with redshifts 2.5, 3.5 and 4.0; and we represent the HzRGs from Table 5. This model allows to differentiate between normal galaxies and starbursts since there is an offset between the models for each of these types of galaxy, as it can be seen in Figure 23.

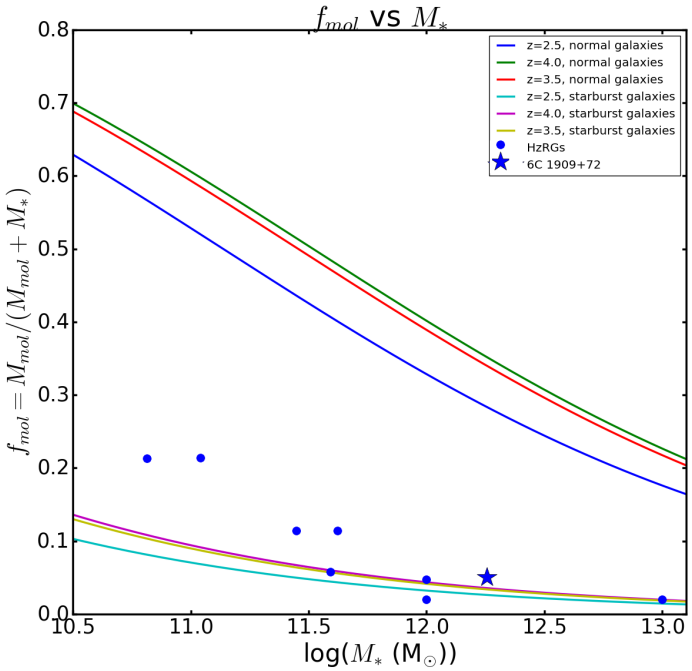

Figure 23: Molecular gas fraction represented as a function of the logarithm of the stellar mass. The dots represent HzRGs, while the star represents 6C 1909+72. The lines at the top of the plot correspond to the values of the model presented in Sargent et al. (2014) for normal galaxies between redshifts 2.5 and 4.0; while the lines at the bottom of the plot correspond to the same model but for starbursts galaxies in the same range of redshifts. The vertical line represents the values of the molecular gas fraction that a galaxy with the same stellar mass as 6C 1909+72 would have according to the different models.

In this plot, it can be seen that 6C 1909+72 follows the model for starburst galaxies, as it could be expected. However, it can also be seen that some of the HzRGs present higher values of the molecular gas fraction that the ones expected for their stellar mass, although they follow the typical tendency for starbursts galaxies. This could be due to the use of an incorrect brightness temperature ratio while obtaining the molecular gas mass; since using a smaller $r_{4-3/1-0}$ would lead to an overestimation of the molecular gas mass; which in turn would mean that the resulting molecular gas fraction would also be overestimated. This is what can be observed in Figure 23, proving that there is not a unique brightness temperature ratio that can be used for all HzRGs and that the use of the one presented in Bothwell et al. (2013) would lead to significant overestimations of the CO (1-0) luminosity. In contrast, 6C 1909+72 does not deviate from the distribution, since its molecular gas mass was obtained using the brightness temperature ratio that Ivison et al. (2012) found specifically for this galaxy.

5 Conclusions

In this work, we studied one of the most puzzling characteristics of HzRGs, the extended (from 50 to 250 kpc) submilimiter emission that has been detected for some of them by Stevens et al. (2003). To explain the mechanishms that could cause this emission, we use observations of the CO (4-3) line from the HzRG 6C 1909+72 at $z = (3.5324 \pm 0.0006)$, which presents one of the most extended submillimeter emission among the ones detected by Stevens et al. (2003), making it one of the best cases for the study of this extended emission.

The main possible scenarios that would explain this extended emission are:

1. Line-of-sight blends, i.e., the emission observed from 6C 1909+72 would actually be the joint emission from it and another galaxy superimposed in the line of sight.
2. Gas-rich mergers: the extended emission would be due to the merging of two or more components.
3. Metal-rich gas and dust entrained in collimated outflows.

Each of the scenarios would be verified in the following cases:

1. The emission from the CO (4-3) transition can be modeled using only a narrow Gaussian profile.
2. The CO (4-3) emission is the emission of all the components, in such a way that, with enough spectral resolution, they could be resolved and the CO (4-3) line could be modeled using two or more narrow Gaussian profiles.
3. The CO (4-3) line can be fitted using a broad Gaussian profile and it presents broad emission wings.

With that, we can find out the scenario that causes the extended submillimeter emission by studying the CO (4-3) line profile. Another way to discern among these scenarios would be studying the emission from the neighbor SMGs; however, they could not be covered in a single pointing of NOEMA, so they were not observed in our case.

Firstly, it is important to point out that our results are consistent with the ones obtained by previous works, like Ivison et al. (2012), but we were able to obtain a SNR a factor 1.75 higher than theirs, assuring the validity of our results. In particular, as a sanity check, we found that the continuum flux we obtained ($S_\nu = (314 \pm 28)$ μJy) is consistent with a SED based on synchrotron and dust emission for dust at $T_d \sim 45$ K.

The CO (4-3) line from 6C 1909+72, after subtracting the continuum from the spectrum, can be successfully fitted using a narrow Gaussian profile with no wings. From this fit, we can conclude that the CO (4-3) line has a full-width at half maximum, FWHM$\sim$ 700 km s^{-1} and its velocity integrated line intensity is: $I_{\mathrm{CO\,(4\text{-}3)}} = (2.62 \pm 0.15)$ Jy km s^{-1}. The redshift of the galaxy obtained using the CO (4-3) line is: $z_{\mathrm{CO\,(4\text{-}3)}} = (3.5328 \pm 0.0002)$, which is more accurate than previous determinations using the same kind of observations.

Following the criteria described by Cicone et al. (2013), since we do not observe any motion of the gas and the CO (4-3) line does not present broad wings and can be fitted using a narrow Gaussian, we can conclude that there are no molecular gas outflows in 6C 1909+72, excluding the third scenario for the origin of the extended submillimeter emission.

To discern between the line-of-sight blends scenario and the merger scenario, we study the possible combinatons of two Gaussian profiles that could reproduce the spectrum. In that way, we find that the CO (4-3) line from 6C 1909+72 can be explained by a model of two unresolved narrow lines with similar properties. These lines would have FWHMs ranging from $\sim$450 to 700 km s^{-1}, which are typival vales for SMGs (Bothwellet al., 2013). However, since there is not a unique combination of the two components and the single Gaussian model provides also a good fit to the line profile, we cannot exclude either of the scenarios. In order to discriminate between them, observations with better spectral resolution would be required.

In addition, we present an extensive compilation of fluxes and properties of 6C 1909+72, as well as a compilation of different HzRGs for which observations of the CO (4-3) line have been carried out so that we can put our target in context.

Among the properties presented for HzRGs, we studied the variations from galaxy to galaxy of the parameter that relates the luminosity of the CO (4-3) line with the luminosity of the CO (1-0) line, the brightness temperature ratio; in such a way that we found that, although this value is different for each HzRGs, it tends to be of the order of 1, in contrast to the value found by Bothwell et al. (2013): $\sim$ 0.4. This implies that the molecular gas in HzRGs is thermalized up

to $J = 4$, while it is not thermalized for the same transitions of SMGs. This could be due to the presence of a source of extra heating of the gas in HzRGs, such us the AGN or the radio jets, as proposed by Ivison et al. (2012). Furthermore, the fact that there is not a unique value of this ratio for all HzRGs is indicative of different environment conditions in each galaxy. With that, we can conclude that it is innapropriate to apply the brightness temperature ratios of SMGs to HzRGs. However, more observations of different transitions of the CO emission from HzRGs are needed in order to determine the brightness temperature ratios of this type of galaxies.

To put our galaxy in context we represent the efficiency of the star-formation, i.e., how efficiently the molecular gas mass is transformed into stars (that gives information of the relation of the SFR with the molecular gas mass using their tracers, the infrared luminosity, and the CO luminosity, and is known as the Schmidt-Kennicutt plot, as shown in Sargent et al., 2014), of the relation of the molecular gas mass with the dynamics of the potential well in which the gas is contained (represented using their tracers, the CO luminosity and the line FWHM, as seen in Bothwell et al., 2013) and, lastly, the evolution of the molecular gas fraction with the stellar mass depending on the redshift of the galaxy, as parametrized by Sargent et al. (2014).

In regards of the Schmidt-Kennicutt plot, we found that, although the HzRGs and the SMGs presented followed the trend expected, we cannot precise which exact model they follow due to the lack of data in our sample and the dispersion found. On the other hand, the QSOs seemed not to follow the expected trend. This could be a result of QSOs having larger brightness temperatures ratios than the rest of the galaxies presented or just a result of the small amount of QSOs in our sample. Another possible explanation could be that the brightness temperature ratio changes more drastically from a QSO to another than for the other kinds of galaxies.

As for the relation of the CO (4-3) luminosity with the FWHM of the line, we were not able to find the same relation as the one presented by Bothwell et al. (2013) for the CO (1-0) line. However, this could be an effect of the small amount of galaxies in our sample. Another possible source of error would be the fact that we used the radius of the CO (1-0) emission for SMGs presented by Ivison et al. (2011) ($\sim$ 7 kpc). This value might not be correct due to the fact that the CO (4-3) transition traces denser and more centrally concentrated gas than the CO (1-0) transition, in such a way that the radius of the emission of the CO (4-3) transition would be much smaller (around $\sim$ 3 kpc for SMGs). Nevertheless, the appropriate value for HzRGs is still unknown since there is just a small number of spatially resolved CO observations for HzRGs.

Lastly, although 6C 1909+72 follows the expected evolution of the molecular gas mass fraction, we observe that most of the HzRGs presented are above the trend that corresponds to them according to their redshift. We conclude that this is a result of the use of inappropriate values for the brightness temperature ratios for these galaxies, since using a smaller $r_{4-3/1-0}$, leads to an overestimation of the molecular gas mass and of the molecular gas mass fraction, hence the importance of the determination of the brightness temperature ratio. In any case, all the HzRGs follow the trend expected for starburst galaxies.

With all that, we can conclude that the use of the same brightness temperature ratio for HzRGs, SMGs, and QSOs leads to overestimations of the molecular gas masses of HzRGs and QSOs. Furthermore, we were able to show that the differences in the gas conditions from a HzRG to another imply that there is not a unique value of this ratio for all HzRGs and more observations of the different CO transitions from HzRGs are needed in order to find the tendency of the variation of this ratio with the properties of the HzRG.

Understanding the process that causes the extended submillimeter emission as well as obtaining more appropriate values for the brightness temperature ratios of the CO transitions for HzRGs will lead us a step closer to understanding the progenitors of the most massive galaxies in the local Universe and, therefore, to understanding better the processes of galaxy evolution.

Name	$z_{\mathrm{CO\ (4-3)}}$	$I_{\mathrm{CO\ (4-3)}}$ (Jy km s^{-1})	FWHM$_{\mathrm{CO\ (4-3)}}$	$L'_{\mathrm{CO\ (4-3)}}$ (K km s^{-1}pc^2)	L_{FIR} (L$_\odot$)	$I_{\mathrm{CO\ (1-0)}}$ (Jy km s^{-1})	$L'_{\mathrm{CO\ (1-0)}}$ (K km s^{-1}pc^2)	$r_{4-3/1-0}$	M_{mol} (M$_\odot$)	M_* (M$_\odot$)	Refs.[a]
6C 1909+72	3.5328 ± 0.0002	2.62 ± 0.15	718 ± 31	(8.8 ± 0.5) · 10^{10}	(4.9 ± 0.9) · 10^{13}	0.22 ± 0.05	(11.9 ± 2.6) · 10^{10}	0.74 ± 0.17	(9.6 ± 2.4) · 10^{10}	∼ 1.8 · 10^{12}	1, 2
B3 J2330+3927	3.0934 ± 0.0005	3.29 ± 0.51	830 ± 100	(8.9 ± 1.4) · 10^{10}	(3.3 ± 0.5) · 10^{13}	<0.074	< 2.9 · 10^{10}	>2.7	∼ 2.3 · 10^{10}	-	2
4C 41.17	3.7958 ± 0.0008	1.8 ± 0.2	1000 ± 150	(6.8 ± 0.8) · 10^{10}	(1.6 ± 0.4) · 10^{13}	-	-	>0.55	∼ 5.4 · 10^{10}	∼ 0.42 · 10^{12}	3, 4
TN J0121+1320	3.517 ± 0.003	1.2 ± 0.4	∼700	(4.0 ± 1.3) · 10^{10}	-	-	-	-	∼ 3 · 10^{10}	∼ 0.11 · 10^{12}	5
4C 60.07	3.7887 ± 0.0007	2.50± 0.43	>1000	(9.4 ± 1.6) · 10^{10}	∼ 1.5 · 10^{13}	0.15 ± 0.03	(9.0 ± 1.8) · 10^{10}	1.04 ± 0.27	< 3.6 · 10^{10}	(0.28 ± 0.12) · 10^{12}	6, 7, 8
8C 1435+635	4.26 ± 0.01	-	∼300	∼ 5 · 10^{10}	∼ 1.0 · 10^{13}	-	< 2.8 · 10^{10}	∼1.79	< 20 · 10^{10}	∼ 10 · 10^{12}	9, 10
B2 0902+34	3.397 ± 0.001	<0.7	∼250	< 2.2 · 10^{10}	-	-	-	-	< 1.76 · 10^{10}	< 6.5 · 10^{10}	11
4C 23.56	2.479 ± 0.001	<1.6	∼250	< 3 · 10^{10}	(2.0 ± 0.5) · 10^{13}	-	-	-	< 2.4 · 10^{10}	< 0.39 · 10^{12}	11, 12
MG 2141+19	3.594 ± 0.003	<2.0	∼250	< 7 · 10^{10}	-	-	-	-	(5.5 ± 0.3) · 10^{10}	-	11
4C +03.24	3.5856 ± 0.001	<0.4	-	< 1.3 · 10^{10}	(0.64 ± 0.14) · 10^{13}	-	< 6.5 · 10^{10}	∼0.2	< 5 · 10^{10}	∼ 1 · 10^{12}	4, 10, 13
Spiderweb	2.1613 ± 0.0001	1.77± 0.09	610 ± 10	(4.4 ± 0.2) · 10^{10}	∼ 1.0 · 10^{13}	0.11 ± 0.03	(2.6 ± 0.7) · 10^{10}	1.00 ± 0.28	(2.0 ± 0.6) · 10^{10}	∼ 1 · 10^{12}	14, 15, 16

Comparison of the properties of different HzRGs for which observations of the CO (4-3) line had been carried out. The properties shown in the table are the following (from left to right): the redshift of the CO (4-3) line, $z_{\mathrm{CO\ (4-3)}}$; the velocity-integrated line intensity, $I_{\mathrm{CO\ (4-3)}}$; the full-width at half maximum of the CO (4-3) line, FWHM$_{\mathrm{CO\ (4-3)}}$; the luminosity of the CO (4-3) line, $L'_{\mathrm{CO\ (4-3)}}$; the infrared luminosity, L_{IR}; the velocity-integrated intensity of the CO (1-0) line, $I_{\mathrm{CO\ (1-0)}}$; the luminosity of the CO (1-0) line, $L'_{\mathrm{CO\ (1-0)}}$; the brightness temperature ratio, $r_{4-3/1-0}$; the molecular mass, M_{mol}; and the stellar mass, M_*. [a]References: 1 = This work; 2 = Ivison et al. (2012); 3 = De Breuck et al. (2005); 4 = Smail et al. (2012); 5 = De Breuck, Neri & Omont (2003); 6 = Ivison et al. (2008); 7 = Papadopoulos et al. (2000); 8 = Greve et al. (2004); 9 = Ivison et al. (1998); 10 = Van Ojik et al. (1996); 11 = Evans et al. (1996); 12 = Humphrey et al. (2011); 13 = Youichi & Yoshiaki (2004); 14 = Emonts et al. (2018); 15 = Miley et al. (2006); 16 = Dannerbauer et al. (2014).

Table 5

Photometric Band	Flux Density	Telescope (Instrument)	Reference
F702W	(8.18 ± 0.16) μJy	HST (WFPC2)	Smith et al. (2010)
K_S	(134 ± 7) μJy	Subaru (CISCO)	Smith et al. (2010)
K_S (line-corrected)	(109 ± 11) μJy	Subaru (CISCO)	Smith et al. (2010)
$S_{3.6\mu m}$	(200 ± 20) μJy	Spitzer (IRAC)	Seymour et al. (2007)
$S_{4.5\mu m}$	(229 ± 23) μJy	Spitzer (IRAC)	Seymour et al. (2007)
$S_{5.8\mu m}$	(241 ± 25) μJy	Spitzer (IRAC)	Seymour et al. (2007)
$S_{8.0\mu m}$	(480 ± 48) μJy	Spitzer (IRAC)	Seymour et al. (2007)
$S_{12\mu m}$	(840 ± 100) μJy	ISO (ISOCAM)	Siebenmorgen et al. (2004)
$S_{16\mu m}$	(1.32 ± 0.07) mJy	Spitzer (IRS)	Seymour et al. (2008)
$S_{24\mu m}$	(1.91 ± 0.10) mJy	Spitzer (MIPS)	Seymour et al. (2007)
$S_{70\mu m}$	(16.2 ± 1.9) mJy	Spitzer (MIPS)	Seymour et al. (2007)
$S_{100\mu m}$	(17 ± 3) mJy	Herschel (PACS)	Ivison et al. (2012)
$S_{160\mu m}$	(34.9 ± 6.5) mJy	Herschel (PACS)	Ivison et al. (2012)
$S_{160\mu m}$	$<$ 63.3 mJy	Spitzer (MIPS)	Seymour et al. (2007)
$S_{250\mu m}$	(57.2 ± 2.7) mJy	Herschel (SPIRE)	Ivison et al. (2012)
$S_{350\mu m}$	(69.6 ± 2.8) mJy	Herschel (SPIRE)	Ivison et al. (2012)
$S_{350\mu m}$	(90 ± 15) mJy	CSO (SHARC-II)	Greve, Ivison & Stevens (2006)
$S_{450\mu m}$	(33 ± 17) mJy	JCMT (SCUBA)	Reuland et al. (2004)
$S_{500\mu m}$	(63.4 ± 3.3) mJy	Herschel (SPIRE)	Ivison et al. (2012)
$S_{850\mu m}$	(34.9 ± 3.0) mJy	JCMT (SCUBA)	Stevens et al. (2003)
$S_{850\mu m}$	(13.5 ± 1.3) mJy	JCMT (SCUBA)	Papadopoulos et al. (2000)
$S_{1250\mu m}$	$<$ 3 mJy	IRAM (PdBI)	Papadopoulos et al. (2000)
$S_{3\ mm}$	$\leq$ 0.6 mJy	IRAM (PdBI)	Papadopoulos et al. (2000)
$S_{3\ mm}$	(0.31 ± 0.03) mJy	IRAM (NOEMA)	Our result
$S_{CO\ (1-0)}$	(0.26 ± 0.04) mJy	NRAO (JVLA)	Ivison et al. (2012)
$I_{CO\ (1-0)}$	(0.222 ± 0.049) Jy km s^{-1}	NRAO (JVLA)	Ivison et al. (2012)
$S_{CO\ (4-3)}$	(3.3 ± 0.3) mJy	IRAM (PdBI)	Ivison et al. (2012)
$S_{CO\ (4-3)}$	(3.42 ± 0.13) mJy	IRAM (NOEMA)	Our result
$I_{CO\ (4-3)}$	(2.69 ± 0.27) Jy km s^{-1}	IRAM (PdBI)	Ivison et al. (2012)
$I_{CO\ (4-3)}$	(1.62 ± 0.30) Jy km s^{-1}	IRAM (PdBI)	Papadopoulos et al. (2000)
$I_{CO\ (4-3)}$	(2.62 ± 0.17) Jy km s^{-1}	IRAM (NOEMA)	Our result

Table 6: Compilation of fluxes from the galaxy in different photometric bands. The reference of each value is listed in the last column, after the telescope and the instrument with which the observations in each case were obtained.

Property	Value	Reference
$z_{\mathrm{CO\ (1\text{-}0)}}$	3.5324 ± 0.0007	Ivison et al. (2012)
$z_{\mathrm{CO\ (4\text{-}3)}}$	3.5324 ± 0.0006	Ivison et al. (2012)
$z_{\mathrm{CO\ (4\text{-}3)}}$	3.532 ± 0.006	Papadopoulos et al. (2000)
$z_{\mathrm{CO\ (4\text{-}3)}}$	3.5328 ± 0.0002	Our result
$z_{Ly\alpha}(I)$	3.5334 ± 0.0008	Smith et al. (2010)
$z_{Ly\alpha}(II)$	3.5363 ± 0.0005	Smith et al. (2010)
$\mathrm{FWHM_{CO\ (1\text{-}0)}}$	(570 ± 90) km s^{-1}	Ivison et al. (2012)
$\mathrm{FWHM_{CO\ (4\text{-}3)}}$	(800 ± 90) km s^{-1}	Ivison et al. (2012)
$\mathrm{FWHM_{CO\ (4\text{-}3)}}$	(530 ± 70) km s^{-1}	Papadopoulos et al. (2000)
$\mathrm{FWHM_{CO\ (4\text{-}3)}}$	(718 ± 31) km s^{-1}	Our result
$L'_{\mathrm{CO\ (4\text{-}3)}}$	$(8.8 \pm 0.5)\cdot 10^{10}$ K km s^{-1}pc^2	Our result
$L'_{\mathrm{CO\ (1\text{-}0)}}$	$(1.19 \pm 0.26)\cdot 10^{11}$ K km s^{-1}pc^2	Ivison et al. (2012)
$L'_{\mathrm{CO\ (1\text{-}0)}}$	$(2.1 \pm 0.4)\cdot 10^{11}$ K km s^{-1}pc^2	Our result, using $r_{43/10} = (0.41 \pm 0.07)$ from Bothwell et al. (2013)
$L'_{\mathrm{CO\ (1\text{-}0)}}$	$(1.2 \pm 0.3)\cdot 10^{11}$ K km s^{-1}pc^2	Our result, using $r_{43/10} = (0.76 \pm 0.18)$ from Ivison et al. (2012)
$r_{43/10}$	(0.74 ± 0.17)	Our result, using $I_{\mathrm{CO\ (1\text{-}0)}}$ from Ivison et al. (2012)
$\log(L_{IR}(L_\odot))$	(13.69 ± 0.08)	Ivison et al. (2012)
L_{FIR}	$\sim 1.5 \cdot 10^{13}$ L$_\odot$	Papadopoulos et al. (2000)
L_{FIR}	$(2.3 \pm 0.4) \cdot 10^{13}$ L$_\odot$	Seymour et al. (2008)
α_{CO}	$0.8\ \mathrm{M_\odot}\left(\mathrm{K\ km\ s^{-1}\ pc^2}\right)^{-1}$	Downes & Solomon (1998)
M_{gas}	$\sim 10^{11}$ M$_\odot$	Ivison et al. (2012)
M_{gas}	$\geq 4.5 \cdot 10^{10}$ M$_\odot$	Papadopoulos et al. (2000)
M_{gas}	$\sim 2.4 \cdot 10^{11}$ M$_\odot$	Stevens et al. (2003) (using gas-to-dust ratio of 200)
M_{gas}	$(1.7 \pm 0.3)\cdot 10^{11}$ M$_\odot$	using $r_{43/10} = (0.41 \pm 0.07)$ from Bothwell et al. (2013)
M_{gas}	$(0.96 \pm 0.24)\cdot 10^{11}$ M$_\odot$	using $r_{43/10} = (0.76 \pm 0.18)$ from Ivison et al. (2012)
M_*	$\sim 1.8 \cdot 10^{12}$ M$_\odot$	Smith et al. (2010)
$\log(M_*(M_\odot))$	< 12.27	Seymour et al. (2007)
M_d	$\sim 1.2 \cdot 10^9$ M$_\odot$	Stevens et al. (2003) ($T_d = 40$ K)
$\log(M_d(M_\odot))$	(9.37 ± 0.04)	Ivison et al. (2012) ($T_d = (45.7 \pm 1.3)$ K)
M_d	$\sim 1.5 \cdot 10^8$ M$_\odot$	Papadopoulos et al. (2000) ($T_d = 50$ K)
M_d	(8 ± 2) M$_\odot$	Seymour et al. (2008) ($T_d = (50 \pm 5)$ K)
M_d	$(3.2 \pm 0.8)\cdot 10^8$ M$_\odot$	Our result (using $r_{43/10} = (0.76 \pm 0.18)$ and a gas-to-dust ratio of 300)
SFR_{IR}	~ 1500 M$_\odot$yr^{-1}	Papadopoulos et al. (2000)
SFR_{IR}	~ 500 M$_\odot$yr^{-1}	Ivison et al. (2012) ($\sim 90\%$ of L_{IR} is due to the AGN activity)
$SFR_{Salpeter\ IMF}$	~ 300 M$_\odot$yr^{-1}	Smith et al. (2010)
$SFR_{Scalo\ IMF}$	~ 680 M$_\odot$yr^{-1}	Smith et al. (2010)
SFR_{FIR}	(4000 ± 700) M$_\odot$yr^{-1}	Seymour et al. (2008)
M_{gas}/M_*	~ 0.05	using $r_{43/10} = (0.76 \pm 0.18)$ and M_* from Smith et al. (2010)
M_{gas}/M_{dust}	(42 ± 11)	using $r_{43/10} = (0.76 \pm 0.18)$ and M_{dust} from Ivison et al. (2012)
f_{mol}	~ 0.05	using $r_{43/10} = (0.76 \pm 0.18)$ and M_* from Smith et al. (2010)

Table 7: Collection of the properties of the galaxy. The references of the data are shown in the last column of the table.

References

[1] Castro-Carrizo A. Absolute flux calibration. In *9th IRAM Interferometry School*, Grenoble, 2016.

[2] Dey A. et al. Triggered Star Formation in a Massive Galaxy at z = 3.8: 4C 41.17. *The Astrophysical Journal*, 490(2):698–709, dec 1997.

[3] Evans A. et al. A Search for CO Emission in High-Redshift Powerful Radio Galaxies. *The Astrophysical Journal*, 457:658, 1996.

[4] Humphrey A. et al. AzTEC 1.1 mm images of 16 radio galaxies at 0.5. *Monthly Notices of the Royal Astronomical Society*, 418(1):74–89, November 2011.

[5] Emonts B. et al. Giant galaxy growing from recycled gas: ALMA maps the circumgalactic molecular medium of the Spiderweb in [CI]. *Monthly Notices of the Royal Astronomical Society*, 477(1):L60–L65, June 2018.

[6] Gullberg B. *Exploring Star Formation in high-z Galaxies using Atomic and Molecular Emission Lines*. PhD thesis, Faculty of Physics, Ludwig–Maximilians–University, Munich, 2016.

[7] Peterson B. and Wilkes B. *Encyclopedia of Astronomy & Astrophysics*, volume 581, chapter Active Galaxies: Unified Model, pages 197–204. Institute of Physics Publisher, December 2006.

[8] Carilli C. and Walter F. Cool Gas in High Redshift Galaxies. *Annual Review of Astronomy and Astrophysics*, 51(1):105–161, August 2013.

[9] Cicone C. et al. Massive Molecular Outflows and Evidence for AGN Feedback from CO Observations. *Astronomy & Astrophysics*, 562(A21), February 2013.

[10] De Breuck C. et al. Detection of Two Massive CO Systems in 4C 41.17 at z = 3.8. *Astronomy and Astrophysics*, 430:L1–L4, January 2005.

[11] Downes D. and Solomon P. M. Rotating Nuclear Rings and Extreme Starbursts in Ultraluminous Galaxies. *The Astrophysical Journal*, 507:615–654, November 1998.

[12] Smith D. et al. When galaxies collide: understanding the broad absorption-line radio galaxy 4C +72.26. *Monthly Notices of the Royal Astronomical Society*, 404:1089–1099, 2010.

[13] Wilner D. Radio Astronomy and Interferometry Fundamentals. In *Swinburne University, lectures on Radio Astronomy*, 2015.

[14] Neri R. De Breuck C. and Omont A. CO Emission from z>3 Radio Galaxies. *New Astronomy Reviews*, 47(4-5):285–289, September 2003.

[15] Gueth F. Calibration principles. In *9th IRAM Interferometry School*, Grenoble, 2016.

[16] Bisbas T. G. et al. Effective destruction of co by cosmic rays: Implications for tracing H2 gas in the universe. *Astrophysical Journal*, 803, April 2015.

[17] Bisbas T. G. et al. Cosmic-ray induced destruction of CO in star-forming galaxies. *The Astrophysical Journal*, 839(2), April 2017.

[18] Miley G. and C. De Breuck. Distant radio galaxies and their environments. *Astronomy and Astrophysics Review*, 15:67–144, 2008.

[19] Miley G. et al. The Spiderweb Galaxy: A Forming Massive Cluster Galaxy at z ˜ 2. *The Astrophysical Journal*, 650(1):L29–L32, oct 2006.

[20] Ivison R. Greve T. and Papadopoulos P. Detection of CO J = 1–0 in the z = 3.79 radio galaxy 4C 60.07. *Astronomy & Astrophysics*, 419(1):99–107, may 2004.

[21] Dannerbauer H. et al. An excess of dusty starbursts related to the Spiderweb galaxy. *Astronomy & Astrophysics*, 570:A55, oct 2014.

[22] Dannerbauer H. et al. The implications of the surprising existence of a large, massive CO disk in a distant protocluster. *Astronomy & Astrophysics*, 608(A48), 2017.

[23] Smail I. et al. Inverse Compton X-ray halos around high-z radio galaxies: a feedback mechanism powered by far-infrared starbursts or the cosmic microwave background? *The Astrophysical Journal*, 760(2):132, dec 2012.

[24] Geach J. et al. Stellar feedback as the origin of an extended molecular outflow in a starburst galaxy. *Nature*, 516(7529):68–70, December 2014.

[25] Stevens J. et al. The formation of cluster elliptical galaxies as revealed by extensive star formation. *Nature*, 425:264–267, September 2003.

[26] R. Kennicutt. The star formation law in galactic disks. *The Astrophysical Journal*, 344:685–703, September 1989.

[27] Aravena M. et al. Cold molecular gas in massive disk galaxies at z=1.5. *The Astrophysical Journal*, 718(1):177–183, May 2010.

[28] Hayashi M. et al. A starbursting proto-cluster in making associated with a radio galaxy at z = 2.53 discovered by Hα imaging. *Astrophysical Journal*, 757(15), September 2012.

[29] Reuland M. et al. Dust and star formation in distant radio galaxies. *Monthly Notices of the Royal Astronomical Society*, 353(2):377–390, 2004.

[30] Sargent M. et al. Regularity underlying complexity: A redshift-independent description of the continuous variation of galaxy-scale molecular gas properties in the mass-star formation rate plane. *Astrophysical Journal*, 793(19), September 2014.

[31] Schmidt M. The rate of star formation. *The Astrophysical Journal*, 129(2):243–258, 1959.

[32] Seymour N. et al. The Massive Hosts of Radio Galaxies Across Cosmic Time. *The Astrophysical Journal Supplement Series*, 171(2):353–375, August 2007.

[33] Seymour N. et al. Mid-Infrared Spectra of High-Redshift (z $>$ 2) Radio Galaxies. *The Astrophysical Journal*, 681(1):L1–L4, jul 2008.

[34] R. Neri. The NOrthern Extended Millimeter Array NOEMA. In *9th IRAM Interferometry School*, 2016.

[35] Papadopoulos P. et al. CO (4-3) and dust emission in two powerful high-z radio galaxies and CO lines at high redshift. *THE ASTROPHYSICAL JOURNAL*, 528:626–636, 2000.

[36] Solomon P. and Bout P. Molecular Gas at High Redshift. *Annual Review of Astronomy & Astrophysics*, 43(1):677–725, September 2005.

[37] V. Piétu. Calibration in practice. In *8th IRAM Interferometry School*, Grenoble, 2012.

[38] Ivison R. et al. Dust, Gas, and the Evolutionary Status of the Radio Galaxy 8C 1435+635 at z = 4.25. *The Astrophysical Journal*, 494(1):211–217, feb 1998.

[39] Ivison R. et al. Interferometric imaging of the high-redshift radio galaxy, 4C60.07: An SMA, Spitzer and VLA study reveals a binary AGN/starburst. *Monthly Notices of the Royal Astronomical Society*, 390(3):1117–1126, November 2008.

[40] Ivison R. et al. Gas-rich mergers and feedback are ubiquitous amongst starbursting radio galaxies, as revealed by the VLA, IRAM PdBI and Herschel. *Monthly Notices of the Royal Astronomical Society*, 425:1320–1331, 2012.

[41] Ivison R. et al. Tracing the molecular gas in distant submillimetre galaxies via CO(1–0) imaging with the EVLA. *Mon. Not. R. Astron. Soc*, 412(3):1913–1925, April 2018.

[42] Overzier R. The realm of the galaxy protoclusters: A review. *Astronomy & Astrophysics Review*, 24(1), November 2016.

[43] Siebenmorgen R. et al. ISOCAM survey and dust models of 3CR radio galaxies and quasars. *Astronomy & Astrophysics*, 421(1):129–145, jul 2004.

[44] Bothwell M. S. et al. A survey of molecular gas in luminous sub-millimetre galaxies. *Monthly Notices of the Royal Astronomical Society*, 429:3047–3067, 2013.

[45] Muldrew S. et al. What are Protoclusters? Defining High Redshift Galaxy Clusters and Protoclusters. *Monthly Notices of the Royal Astronomical Society*, 452(3):2528–2539, September 2015.

[46] Greve T., Ivison R., and Stevens J. 350 um sharc-ii imaging of luminous high-redshift radio galaxies. *Astronomische Nachrichten*, 327(2/3):208–212, 2006.

[47] Moran J. M. Thompson A. and Swenson G. W. *Interferometry and Synthesis in Radio Astronomy*. Springer Open, 2017.

[48] Beckmann V. and Shrader C. *Active Galactic Nuclei*. Wiley, 2012.

[49] W. Van Breugel. The Highest Redshift Radio Galaxies. In SPIE, editor, *Discoveries and Research Prospects from 8- to 10-Meter-Class Telescopes*, volume 4005, pages 83–94, June 2000.

[50] van Ojik R. et al. A search for molecular gas in high redshift radio galaxies. *Astronomy and Astrophysics*, 321:389–396, May 1996.

[51] Van Breugel W. et al. Very High Redshift Radio Galaxies. In Faffaella Morganti and Warrick J. Couch, editors, *Looking Deep in the Southern Sky, Proceedings of the ESO/Australia Workshop*, 1998.

[52] Ohyama Y. and Taniguchi Y. Subaru Spectroscopy of the Giant Ly Nebula Associated with the High-z Powerful Radio Galaxy 1243+036. *The Astronomical Journal*, 127(3):1313–1317, mar 2004.